nature microbiology

Article

https://doi.org/10.1038/s41564-025-02087-4

Pseudomonas aeruginosa senses exopolysaccharide trails using type IV pili and adhesins during biofilm formation

Received: 15 November 2024

Accepted: 12 July 2025

Published online: 05 September 2025

Check for updates

William C. Schmidt[1,2,3,4,8], Calvin K. Lee[1,2,3,4,8], Xuhui Zheng[5], Jonathan W. Chen[1,2,3,4], Kirsten L. Fetah[1], James R. Popoli[1], Yun Su Choi[3], Thomas D. Young[2,4], Paul S. Weiss[1,2,4,6], Andrea M. Kasko[1,4], George A. O'Toole[7] ✉, Matthew R. Parsek[5] ✉ & Gerard C. L. Wong[1,2,3,4] ✉

During early stages of biofilm formation, *Pseudomonas aeruginosa* (Pa) PAO1 can sense exopolysaccharide (EPS) trails of Psl deposited on a surface by previous Pa cells to detect trajectories of other cells and to orchestrate motility. This sensory signal is transduced into cyclic diGMP second messengers, but no known Psl receptors and adhesins participate in signal transduction. Here, using bacteria-secreted Psl trails, glycopolymer-patterned surfaces, longitudinal cell tracking, second messenger dual reporters and genetic mutations targeting EPS binding and surface twitching, we find that Pa is capable of sensing EPS directly through mutually constitutive interactions between type IV pili (T4P)-powered twitching and specific adhesin–EPS bonds. This unanticipated mechanochemical surveillance of the Pa environment, where T4P pull against cell-body localized adhesins interacting with EPS trails, such as mannose-binding CdrA, generates a hybrid, transitional planktonic-to-biofilm population with elevated cyclic diGMP and elevated cyclic AMP, as well as increased motility capable of following EPS trails. These results show a generalizable mechanism of surface chemosensing through mechanosensitive appendages.

Pseudomonas aeruginosa (Pa) is a biofilm-forming opportunistic pathogen commonly found in respiratory infections such as cystic fibrosis[1]. As part of its life cycle, Pa produces biofilms by secreting matrix components such as exopolysaccharides (EPS), extracellular DNA and proteins[2–4]. In the PAO1 serotype, the primary EPS for biofilm formation is the Psl polysaccharide, composed primarily of mannose alongside other saccharides[5–7]. The production of these matrix components is mediated by the intracellular second messenger small-molecule cyclic diGMP (cdGMP)[8–10]. cdGMP also mediates a series of behavioural transitions following surface attachment, with the cells progressing from reversible attachment to irreversible attachment as increasing cdGMP expression drives surface commitment[8,11–13]. While on a surface, Pa undergoes translational motility mediated by its type IV pili (T4P), referred to as 'twitching' motility[14,15]. Both the T4P and twitching motility are regulated by cyclic AMP (cAMP)[11,12,16], another crucial second messenger signal in surface attachment, exploration

[1]Department of Bioengineering, University of California, Los Angeles, Los Angeles, CA, USA. [2]Department of Chemistry and Biochemistry, University of California, Los Angeles, Los Angeles, CA, USA. [3]Department of Microbiology, Immunology, & Molecular Genetics, University of California, Los Angeles, Los Angeles, CA, USA. [4]California NanoSystems Institute, University of California, Los Angeles, Los Angeles, CA, USA. [5]Department of Microbiology, University of Washington, Seattle, WA, USA. [6]Department of Materials Science and Engineering, University of California, Los Angeles, Los Angeles, CA, USA. [7]Department of Microbiology and Immunology, Geisel School of Medicine at Dartmouth, Hanover, NH, USA. [8]These authors contributed equally: William C. Schmidt, Calvin K. Lee. ✉e-mail: georgeo@dartmouth.edu; parsem@u.washington.edu; gclwong@seas.ucla.edu

and commitment. Previous studies have shown that during twitching motility, PAO1 secretes Psl trails that guide the formation of future microcolonies on the surface[17]. It has also been shown that Psl can drive increased cdGMP production in Pa via the upregulation of associated diguanylate cyclases such as SiaD[18]. However, it remains unclear how this Psl-mediated cdGMP expression is achieved. It is equally unclear how such EPS sensing relates to control of T4P-driven surface motility necessary for depositing trails, especially as T4P activity depends on cAMP, another second messenger related to surface sensing, but with no known link to EPS sensing[11,12]. Connecting intercellular EPS-mediated bacterial signalling with intracellular second messenger signals and how this interconnection impacts biofilm formation has been a long-standing challenge.

One of the key structural difficulties that has prevented direct studies of naturally produced, surface-associated EPS trails is their spatial and temporal heterogeneity, which is further compounded by the lack of knowledge on how particular EPS saccharide motifs induce specific bacterial responses. To elucidate the effects of trails on bacterial localization, surface motility and second messenger production, we microfabricated geometrically defined surface trails grafted with synthetic glycomimetic polymers. By using these surfaces with a combination of longitudinal flow cell experiments, dual reporters for cAMP and cdGMP, and targeted mutations in systems associated with EPS binding and surface twitching, we find that EPS sensing on a surface is derived from the interactions of three necessary cellular factors to drive both cAMP and cdGMP signalling. Interactions between cell-surface adhesins and surface-deposited EPS generate a resistive force to twitching, which can then be transduced via the T4P mechanosensing apparatus into second messenger signals. This results in a highly tunable system, in which changes in the surface chemistry, the concentration and presentation of cell surface adhesins, and the number and behaviour of the T4P can fundamentally change the second messenger expression of an individual cell, altering cAMP and cdGMP expression in distinct but interdependent mechanisms. It also allows for future cells to sense and respond to the EPS depositions of progenitor exploratory cells, effectively allowing intergenerational communication of environmental characteristics for more efficient future surface colonization and biofilm formation. The generalizability and modularity of such a system would allow for the potential detection of multiple surface chemical features simultaneously via different cell surface adhesins, which would all be sensed and transduced through T4P mechanosensing, without the need of dedicated traditional two-component sensors.

Results

Native and artificial EPS trails both drive surface behaviour

To study the effects of surface-associated EPS on bacterial sensing and behavioural response, we have developed a method of patterning a glass surface with highly geometrically defined surface trails grafted with synthetic glycomimetic polymers presenting saccharide side chains for bacterial interaction (Fig. 1a). This approach has the added advantage of controlling specific stereochemical presentation of EPS moieties (Methods and Supplementary Discussion). We first examined mannose motifs as they are the most abundant monosaccharide component of Psl (Fig. 1a and Extended Data Fig. 1)[7]. Specifically, the α-D-mannose stereoisomer has been shown to be a side chain of the main polysaccharide backbone, similar to our polymer design[7], and PAO1 has been shown to bind to the α-D-mannose of Psl consistently and significantly[19]. Pa recognition of mannosyl residues may additionally be important in an infection model due to the high prevalence of mannose residues present on some cell types and its importance in facilitating bacterial attachment to such cells[20]. In combination with flow cell tracking and a dual cAMP and cdGMP reporter plasmid[12,13,21], we monitored second messenger expression and surface motility in response to interactions with both naturally produced Psl trails and artificial 'polymannose' trails.

Wild-type cells prefer revisiting regions with secreted trails (Fig. 1b,c, left, and Extended Data Fig. 2, left column), defined as trails that have been previously deposited by surface-attached cells (Methods). This result is consistent with previous work that has shown that visit frequencies track with amounts of secreted Psl (ref. 17). To examine surface behaviour as a function of trail chemistry, we compared the relative surface coverage on regions with trails (that is, 'on' trail) to regions lacking trails (that is, 'off' trail) (Fig. 1d), normalized by the surface area of each. Integrating this curve leads to a trail preference index (TPI, Fig. 1e) that measures preference for being on or off a trail. Cells have a TPI for their own secreted Psl slightly above the no-preference baseline (Fig. 1d,e), consistent with previous observations[17]. Next, we examined how cells interact with natural trails compared with synthetic trails with defined concentrations of mannose motifs (Methods)[22]. Here cells conform more to the trail geometry (Fig. 1b,c, centre, and Extended Data Fig. 2, centre column), with a greater TPI (Fig. 1d,e). When naturally secreted Psl trails are removed via the Δ*pslBCD* mutant, cells prefer polymannose trails even more strongly (Fig. 1b,c, right, and Extended Data Fig. 2, right column), with an even higher TPI (Fig. 1d,e). Interestingly, these conditions are not statistically different from each other, which means that although bacteria have a slightly higher affinity for synthetic polymannose trails than naturally produced trails, the impact of the two types of trails on bacterial interactions is comparable.

Surface EPS sensing drives second messenger signalling

Current thinking in the field suggests that bacterial populations that encounter surfaces can be grouped into a low-cdGMP, motile subpopulation and a sessile, biofilm-committed high-cdGMP subpopulation[23–26]. Our analyses of cells that interact with EPS trails reveal an unanticipated second messenger signalling signature distinct from this prevailing dichotomy. To examine how Pa second messenger expression and motility are influenced by EPS trails, we characterized cell surface populations based on the trail type(s) they encounter. Using our EPS-patterned surfaces, cells can encounter artificial polymannose trails, naturally produced native EPS trails, combinations of both and virgin glass surfaces lacking any trails, all within the same flow cell environment (Fig. 2a). In the absence of trails, cells show signal expression and motility representative of early 'pre-biofilm' cells following surface attachment but before secreting their own trails (Fig. 2b–d, black). Contact with either trail type promotes intracellular cdGMP production (Fig. 2b–d, maroon and blue). Interestingly, secreted trails with natural Psl motifs decrease cAMP and twitching (Fig. 2c,d, blue), while artificial polymannose trails increase cAMP and twitching (Fig. 2c,d, maroon). These trail-induced signal and motility responses show that mannose in EPS trails can help to create a non-canonical, pre-biofilm, 'trail-following' subpopulation with increased motility, cAMP and cdGMP as a distinct stage of biofilm development. This increase in motility is in contrast to conventional notions of EPS as a motility-obstructing adhesive and more similar to S-motility behaviours observed in *Myxococcus xanthus* EPS (Supplementary Discussion)[7,27,28]. Interestingly, trail following mostly occurs on spatially extended EPS trails and not on spatially localized EPS patches (Extended Data Fig. 3), suggesting that trail following also depends on trail geometry (Supplementary Discussion). Observations made on surfaces with both artificial polymannose trails and natural secreted trails show that the effect of both trails together is similar to the sum of effects from each individual trail (Fig. 2b–d, cyan). These results also suggest that increased local mannose content on a Psl trail could control Pa behaviour by increasing cdGMP signalling, while cAMP signalling and twitching can be modulated by the presence of multiple saccharides of a Psl trail.

The findings above enable us to define the mechanism underlying EPS sensing on a surface. To understand the mechanism behind mannose sensing, we focus on how artificial polymannose trails change

https://doi.org/10.1038/s41564-025-02087-4

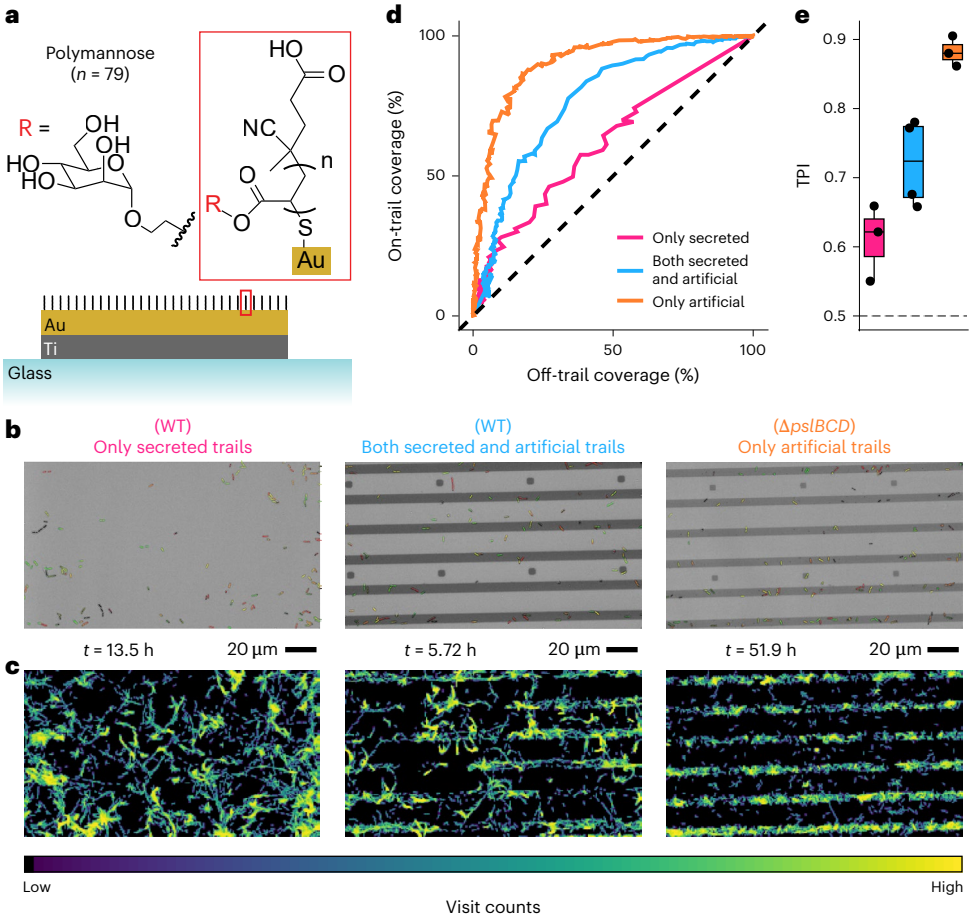

Fig. 1 | Pa interacts with artificial polymannose trails in a similar manner to naturally secreted Psl. a, Schematic diagram of the glycomimetic artificial trails. Glycopolymers are grafted to the lithographically defined patterns via a gold–thiol covalent linkage to form the polymannose trails. **b**, Representative bright-field images of PAO1 on a surface with or without artificial polymannose, overlaid with corresponding cdGMP (green) and cAMP (red) cell reporter signals. Image times correspond to 10% surface coverage. **c**, Visit maps of the images in **b** showing the total cell surface visits within the field of view before the bright-field image at time *t*. **d**, Trail preference curves for the three conditions in **b**, analogous to receiver operating characteristic curves[64]. These results correspond to 'true positive' (a given cell is in contact with the trail) versus 'false positive' (the cell is not on the trail) rates of trail occupancy by cells. Trail preferences are for secreted (pink) and artificial polymannose (blue and orange) trails, respectively. **e**, Taking the area under the curve of **d** yields a trail preference index (TPI) that describes population-level behaviour in response to the surface trails. Trail preference spans from 0 (maximal preference for being 'off' trail) to 1 (maximal preference for being 'on' trail), with 0.5 (black dashed line) being no preference for either. The dots represent the TPI for a single biological replicate, which is defined as a single flow cell experiment (Methods), and the boxes represent the median and interquartile range (IQR) of all biological replicates, with whiskers representing 1.5 IQR. A two-sided Mann–Whitney *U* test with Bonferroni multiple test correction was used (no star, $P \geq 0.05$) for all comparisons. Adjusted *P* values: 0.34 for columns 1 versus 2, 0.30 for columns 1 versus 3, and 0.17 for columns 2 versus 3. Number of biological replicates: WT with only secreted trails (pink, column 1), 3; WT with both trails (blue, column 2), 4; and Δ*pslBCD* with only artificial trails (orange, column 3), 3.

behaviour in key mutants. As some of these mutants do not express natural Psl, we will compare two cases only: on (red) and off (grey) the artificial glycopolymer trail (Fig. 3). As a result, the wild-type (WT) populations present in Fig. 2 have been aggregated into just two populations, based on their relative positions on (Fig. 2 cyan, maroon) and off (Fig. 2 blue, black) artificial trails. We have chosen CdrA, a cell surface adhesin that binds to the mannose moiety of Psl, as our adhesin of interest because of its function in binding and cross-linking Psl, and because it is one of the most well studied adhesins that interact with EPS, showing increased expression in response to cdGMP levels and serving as a cross-linker for the biofilm matrix when released from the cell body[29–32]. CdrA is also known to increase cdGMP expression in response to Psl to promote biofilm formation[18], but the mechanism of this Psl sensing is unclear as CdrA is not a known component of a signal transduction system. Upon deletion of CdrA, we find that the cdGMP increase from contact with the artificial polymannose trail observed for the WT is lost (Fig. 3a), indicating that CdrA–mannose interactions are crucial for transducing binding into increased cdGMP levels. Deletion of CdrA also results in a loss of the trail-induced increase in cAMP (Fig. 3b). While the changes in cAMP between on and off artificial trails in this condition are small, we emphasize that they are statistically significant and reproducible. In fact, it has been shown that small changes in cAMP can result in dramatic changes in motility behaviour[33]. These findings suggest the possibility that additional factors, such as other adhesins and EPS, may play a role in surface motility and cAMP expression.

The trends in cdGMP and cAMP observed in the Δ*cdrA* mutant are largely maintained in a comparison of behaviour on artificial polymannose trails between the WT and Δ*pslBCD*, which does not produce Psl. Interestingly, cdGMP and cAMP levels change in opposite ways to result in the net losses of sensing. The loss of Psl secretion leaves only the CdrA–glycopolymer interaction, reducing the total interaction between the cells and the surface. This results in an increase in the correlated cAMP and twitching phenotypes as well as a reduction in cdGMP signalling. While the cdGMP for the on-trail population drops to the same level as the off-trail population, the off-trail population increases in cAMP to the same level as the on-trail population. In addition, we

https://doi.org/10.1038/s41564-025-02087-4

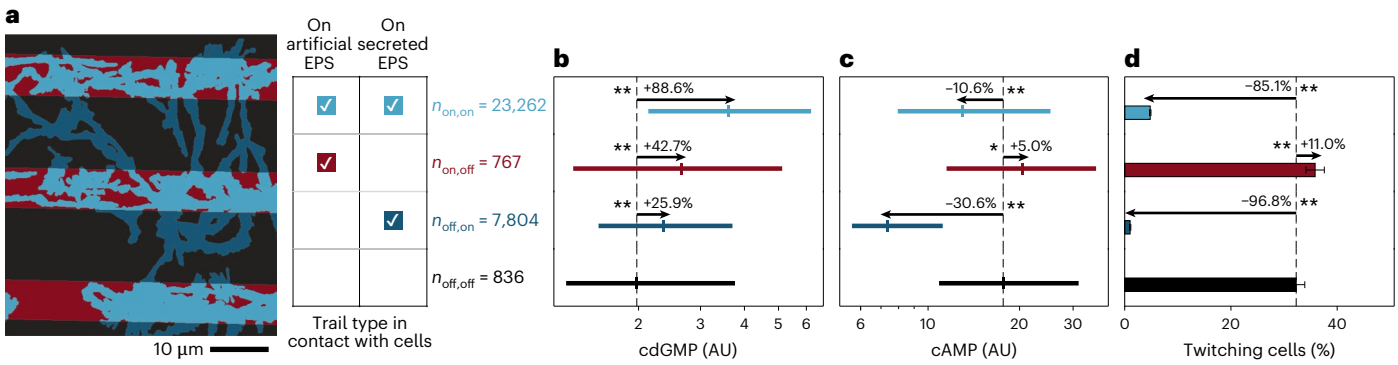

Fig. 2 | Pa exhibits synergistic signalling on artificial and secreted EPS trails. **a**, Representative depiction of artificial trails overlaid with secreted trail deposition from the cell visit map (Fig. 1c, middle). Check marks denote whether a cell is in contact with a given EPS type, which is used to subdivide the population. Cells can be in contact with only artificial polymannose EPS (maroon), only previously deposited naturally secreted Psl (blue), both artificial and secreted EPS in the same location (cyan), or previously unvisited regions without any EPS (black). **b**–**d**, The effect of secreted and/or artificial EPS trails on cdGMP signalling (**b**), cAMP signalling (**c**) and twitching motility (**d**) for the WT. Colours correspond to the subpopulations outlined in **a**. Cells from all four biological replicates have been aggregated together and then subdivided accordingly. Both cdGMP and cAMP have been normalized to the expression of *PrpoD*-SCFP3A, and all fluorescence intensities have been background subtracted. For **b** and **c**, vertical lines represent the median and the whiskers represent the IQR of each subpopulation. For **d**, the bars and whiskers represent the mean and standard deviation of the bootstrap sampling of each subpopulation mean twitching fraction, respectively. The black arrows represent the shift in median compared with the baseline (dashed line; no trail). A two-sided Mann–Whitney *U* test with Bonferroni multiple test correction was used (no star, $P \geq 0.05$; *$P < 0.05$; **$P < 0.001$) for all comparisons (each trail condition versus no trails). Adjusted *P* values (top to bottom): $P = 7.8 \times 10^{-70}$, 2.7×10^{-5}, 4.4×10^{-6} (**b**); $P = 3.5 \times 10^{-19}$, 0.0037, 2×10^{-185} (**c**); $P = 7.6 \times 10^{-34}$, 3.5×10^{-25}, 7.5×10^{-34} (**d**). Number of cells in each subpopulation: both EPS (cyan), 23,262; only artificial EPS (maroon), 767; only secreted EPS (blue), 7,804; and no trails (black), 836. The starting numbers of cells per biological replicate before aggregating and subdividing: WT (*n* = 28,882, 23,445, 18,052, 10,724), Δ*cdrA* (*n* = 20,490, 21,009, 18,011, 25,885), Δ*pslBCD* (*n* = 17,455, 17,350, 16,703, 20,977) and Δ*pilT* (*n* = 15,967, 18,495, 15,720, 14,009).

separate the physicality of binding between the cell surface CdrA and EPS trails from the chemistry of CdrA–mannose binding via the introduction of exogenous methyl-α-D-mannopyranoside (D-Mann), a non-metabolizable mannose analogue which outcompetes natural EPS depositions for CdrA binding[30]. The addition of D-Mann to WT Pa results in a shift in signal profile and residence time towards that of the Δ*pslBCD* mutant, indicative of the role that surface binding plays in mediating these signals (Extended Data Fig. 4). Taken together, these results suggest that mannose sensing results in a 'signalling codon' that creates a trail-following subpopulation with more twitching motility, cAMP and cdGMP.

Importantly, disruption of T4P retraction activity (and, by implication, T4P-driven twitching motility) by deletion of the retraction ATPase (Δ*pilT*) leads to loss of cAMP (Fig. 3b) and, surprisingly, a substantial loss of cdGMP, which is reduced by over an order of magnitude regardless of whether cells are interacting with secreted EPS trails or artificial polymannose trails (Fig. 3a). Although surface residence time can sometimes be a useful metric for tracking cdGMP expression, these observed changes in cdGMP cannot be explained by changes in residence time due to alteration of cell adhesion, as we find that surface residence times between on and off trail in the mutant strains do not correlate with the observed cdGMP signal increases (Extended Data Fig. 5).

The importance of T4P retraction activity in mannose sensing is highlighted in the trail-mediated changes in twitching motility (Fig. 3c). The WT shows an increase in twitching motility on artificial trails, due to surface geometry effects (Extended Data Figs. 3, 6 and 7; Supplementary Video 1; and Supplementary Discussion) and trail-induced increases in cAMP (Figs. 2b and 3a). When either the CdrA adhesin (Δ*cdrA*) or the ability to produce Psl (Δ*pslBCD*) is disrupted, the fraction of twitching cells increases significantly. This increase is probably the result of reduced surface interaction caused by the loss of each half of the binding pair, respectively, resulting in a general reduction in surface interaction strength and an increased motility baseline relative to the WT condition with both natural and artificial trails present. This increased twitching is consistent with the increased cAMP baseline seen

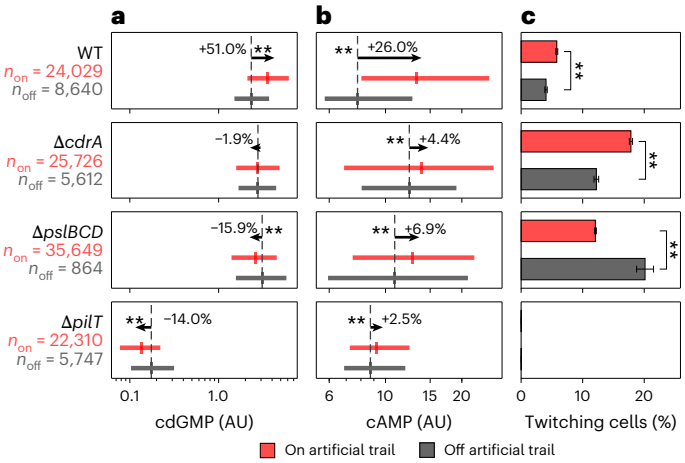

Fig. 3 | CdrA and T4P retraction are required for Pa sensing of EPS trails. **a**–**c**, cdGMP levels (**a**), cAMP levels (**b**) and twitching fraction (**c**) for various mutants whose cell subpopulations are on (red) or off (grey) the artificial polymannose trail patterns. For each mutant, cells from all four biological replicates have been aggregated together and then subdivided accordingly. For **a** and **b**, vertical lines represent the median, the whiskers represent the IQR of each subpopulation and the black arrows represent the shift in median compared with baseline (off artificial trail). For **c**, bars and whiskers represent the mean and standard deviation of the bootstrap sampling of each subpopulation mean twitching fraction, respectively. The inability of the Δ*pilT* strain to retract T4P results in a loss of twitching for the entire population. A two-sided Mann–Whitney *U* test with Bonferroni multiple test correction was used (no star, $P \geq 0.05$; **$P < 0.001$) for all comparisons (on versus off trail). Adjusted *P* values (top to bottom): $P = 2.2 \times 10^{-16}$, 0.24, 4.9×10^{-9}, 8.3×10^{-108} (**a**); $P = 2.2 \times 10^{-16}$, 8.1×10^{-15}, 3.3×10^{-6}, 4.9×10^{-15} (**b**); and $P = 2.5 \times 10^{-34}$, 2.5×10^{-34}, 2.5×10^{-34}, 0.55 (**c**). Number of cells in each subpopulation: WT, 24,029 on and 8,640 off; Δ*cdrA*, 25,726 on and 5,612 off; Δ*pslBCD*, 35,649 on and 864 off; Δ*pilT*, 22,310 on and 5,747 off. The starting numbers of cells per biological replicate before aggregating and subdividing: WT (*n* = 28,882, 23,445, 18,052, 10,724), Δ*cdrA* (*n* = 20,490, 21,009, 18,011, 25,885), Δ*pslBCD* (*n* = 17,455, 17,350, 16,703, 20,977) and Δ*pilT* (*n* = 15,967, 18,495, 15,720, 14,009).

https://doi.org/10.1038/s41564-025-02087-4

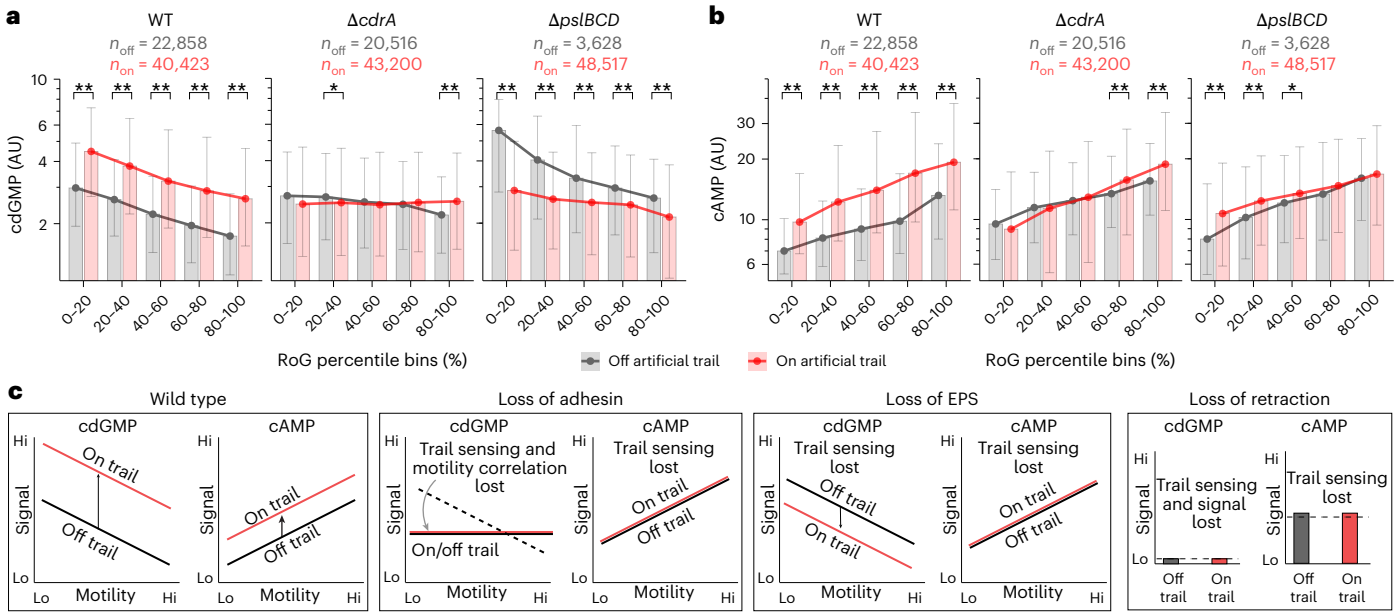

Fig. 4 | CdrA is essential for twitching-based cdGMP signalling. a,**b**, cdGMP–twitching motility (**a**) and cAMP–twitching motility (**b**) correlation plots for WT, Δ*cdrA* and Δ*pslBCD*. On (red) and off (grey) artificial trail cell subpopulations are grouped by RoG percentile bins, with 0% and 100% representing the smallest and largest RoG within a given subpopulation, respectively. RoG is proportional to the average twitching speed. For each mutant, cells from all four biological replicates have been aggregated together and then subdivided accordingly. The lines and bars represent the median cdGMP and cAMP expression for each subpopulation bin, and the error bars represent the IQR of each subpopulation bin. The Δ*pilT* mutant is not included as it has effectively zero cells showing twitching motility (Fig. 3c). For each corresponding comparison of on versus off, a two-sided Mann–Whitney *U* test with Bonferroni multiple test correction was used (no star, $P \geq 0.05$; $^{*}P < 0.05$; $^{**}P < 0.001$). Adjusted *P* values (left to right): WT ($P = 4 \times 10^{-160}$, 7.7×10^{-147}, 4.3×10^{-156}, 1.4×10^{-163}, 1.2×10^{-164}), Δ*cdrA* ($P = 0.076$, 0.005, 1, 0.15, 3.4×10^{-23}), Δ*pslBCD* ($P = 1.9 \times 10^{-54}$, 2.9×10^{-27}, 2.7×10^{-13}, 1.6×10^{-5}, 1.3×10^{-6}) (**a**); WT ($P = 1.7 \times 10^{-199}$, 4.2×10^{-230}, 3.1×10^{-231}, 1×10^{-246}, 2×10^{-132}), Δ*cdrA* ($P = 0.47$, 1, 1, 1.3×10^{-13}, 8.3×10^{-35}), Δ*pslBCD* ($P = 7 \times 10^{-9}$, 1.2×10^{-6}, 0.0074, 0.17, 0.86) (**b**). Number of cells in each subpopulation: WT, 40,423 on and 22,858 off; Δ*cdrA*, 43,200 on and 20,516 off; Δ*pslBCD*, 48,517 on and 3,628 off. The starting numbers of cells per biological replicate before aggregating and subdividing: WT (n = 28,882, 23,445, 18,052, 10,724), Δ*cdrA* (n = 20,490, 21,009, 18,011, 25,885), Δ*pslBCD* (n = 17,455, 17,350, 16,703, 20,977). **c**, Representative diagrams outlining the qualitative changes to cdGMP and cAMP signalling observed in **a** and **b**. Hi and Lo indicate qualitative representations of the cdGMP, cAMP and RoG values exhibited in **a** and **b**. In the WT, both signals increase from contact with the artificial trail, while removal of adhesin or EPS results in loss of trail-induced signal increases. In addition, the signal–motility correlation in cdGMP is lost upon deletion of the surface adhesin. Finally, T4P disruption results in loss of cdGMP expression, cAMP trail sensitivity and motility.

in the off-trail population for these mutants (Fig. 3b). In a Δ*cdrA* mutant strain, the motility increase is greater on trail than off. We hypothesize that this change is due to the greater abundance of mannose motifs on trails that are no longer interacting with CdrA. For the Δ*pslBCD* mutant strain, the motility increase is greater off the trails as there are no mannose motifs from either artificial polymannose or secreted Psl to reduce twitching. Importantly, in a Δ*pilT* mutant strain, cells completely lose cdGMP expression when they are no longer capable of T4P retraction and twitching motility.

Pa coordinates cell behaviour using T4P and CdrA–Psl binding

To investigate the impact and interdependencies between T4P activity, CdrA and Psl on cdGMP and cAMP signalling, we analysed the surface population based on their twitching motility. By measuring the spatial extent of cellular trajectory using radius of gyration (RoG) over a fixed time interval (that is, the fluorescence imaging interval of 5 min), we obtain an effective velocity for surface twitching motility[26,34,35]. We compare the twitching motility of different cells in the population using percentile binning of the RoG values to organize the cells based on their relative twitching motility within their population. We observed that, consistent with previous studies, cAMP and cdGMP positively and negatively correlate with twitching motility, respectively (Fig. 4a,b)[12]. The artificial polymannose trail increases the signal expression across all percentiles without altering these correlations, indicating that saccharide sensing occurs at all levels of surface motility (Fig. 4c). Cells lacking CdrA or Psl lose the trail-induced increase in both signals, with the Δ*pslBCD* mutant showing higher off-trail cdGMP expression. This may be the result of a bias for higher-cdGMP cells, which have a greater chance of additional EPS and adhesin expression to facilitate attachment. However, while the Δ*pslBCD* mutant strain maintains both signal–motility correlations, the Δ*cdrA* strain maintains only the cAMP-motility correlation, with the cdGMP–motility correlation entirely lost.

Discussion

Taken together, the results presented here indicate an EPS saccharide motif sensing mechanism where cAMP expression is dependent on the frequency of T4P retraction[33], and cdGMP expression is dependent on T4P 'frustration', where T4P-driven movement is temporarily stalled by specific adhesin–saccharide surface interactions[36,37], which can occur separately or simultaneously (Fig. 5e). T4P retraction pulls the cell along the surface during twitching motility, with increased frequency of successful retraction events correlating with greater twitching distance and increased cAMP signalling[11,12,38]. By contrast, the binding force between the different distributions of CdrA cell body adhesins and Psl mannose motifs on the surface can frustrate T4P retraction to different degrees, leading to a reduction in twitching distance and an increase in cdGMP signalling, potentially via retraction ATPase stalling. For additional analyses of potential mechanisms for T4P-mediated cAMP and cdGMP expression, see Supplementary Discussion.

We propose that during twitching on bare surfaces, there are insufficient CdrA–mannose/Psl interactions to impede T4P retraction, resulting in expression of only cAMP (Fig. 5a). This case is seen in WT cells off trail (Fig. 2b–d, black), where cells twitch freely with high cAMP.

https://doi.org/10.1038/s41564-025-02087-4

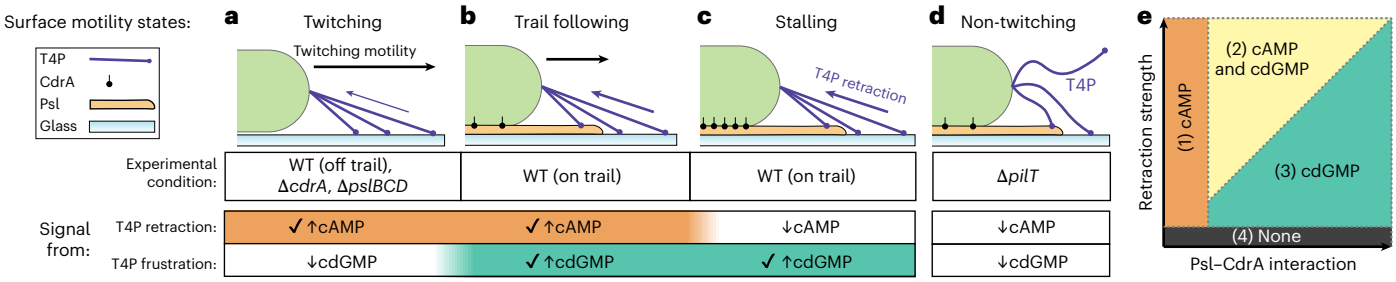

Fig. 5 | Coordinated interactions between T4P, cell adhesins, and EPS drive cAMP and cdGMP expression. a–d, Representative schematics outlining the hypothesized chemo-mechanotransduction pathway involving the interdependence of CdrA–Psl-surface interactions in tandem with T4P mechanosensing. We propose that twitching with minimal surface interactions (below threshold Psl–CdrA interaction) stimulates only cAMP expression via T4P retraction (**a**). Upon encountering surface-deposited EPS, T4P retraction becomes more frustrated (retraction strength greater than Psl–CdrA interaction), leading to both cAMP and cdGMP expression from T4P retraction and frustration, respectively (**b**). As cdGMP increases, CdrA concentration proportionally increases, and when surface interactions become too strong (Psl–CdrA interaction greater than retraction strength), T4P retraction is stalled, leading to a loss of twitching and cAMP generation, while continued T4P frustration from attempting to twitch leads to cdGMP expression (**c**). Finally, if the cell cannot twitch, neither signal is produced in response to T4P-based mechanosensing (below threshold retraction strength) (**d**). **e**, Phase diagram outlining the hypothesized pathways in **a**–**d**. The phase diagram shows increasing Psl–CdrA interaction as the *x*-axis and increasing T4P retraction strength as the *y*-axis. Phase (1) with only cAMP corresponds to **a**, phase (2) with both cAMP and cdGMP corresponds to **b**, phase (3) with only cdGMP corresponds to **c** and phase (4) with no signal corresponds to **d**.

If a trail exists and there is sufficient CdrA–mannose/Psl interaction to resist T4P retraction, then the strength of these interactions controls the spectrum of second messengers expressed (Fig. 5e): when CdrA–mannose/Psl interaction is strong enough to stall T4P retraction, cells cannot twitch and produce only cdGMP as a result of attempting to retract (Fig. 5c). This happens for most cases of WT on secreted trails with mixed saccharides (Fig. 2b,c), resulting in non-twitching cells with low cAMP and high cdGMP. Previous studies have shown that the binding force of T4P to a surface can exceed the retraction force generated by the T4P, indicating the feasibility of this regime[39,40]. Conversely, when T4P retraction overcomes adhesin–saccharide interactions, cells can twitch and produce both cAMP (via T4P retraction) and cdGMP (via frustration of T4P retraction) (Fig. 5b). This case is sometimes observed for WT on secreted trails, but most commonly for WT cells on artificial polymannose trails that interact via CdrA–mannose (Fig. 2b,c), leading to twitching cells with increased levels of both signals. Over time, increased cdGMP levels lead to proportional increases in CdrA production, increasing the cell–EPS interactions and driving the sensory system towards the high-cdGMP stalling condition, leading to surface commitment and biofilm formation.

Disruptions to this process result in alterations to cellular signalling profiles and consequently to biofilm formation. In Pa, cells attach to the surface through a combination of T4P binding, which bring the cell body to the surface, and adhesin–EPS-surface interactions, which anchor the cell onto the surface after sufficient contact time (Supplementary Discussion)[38,41,42]. Cells without Psl (Δ*pslBCD*) show diminished attachment, requiring upwards of 60 h to initiate surface commitment (Extended Data Fig. 2 and Supplementary Discussion). Upon landing, they exclusively interact with the artificial polymannose trail via CdrA present on the cell body (Fig. 5b,c, Extended Data Fig. 7 and Supplementary Video 2). Without the CdrA adhesin (Δ*cdrA*) and/or Psl production (Δ*pslBCD*), T4P dynamics are unaffected but the CdrA–mannose/Psl interactions that oppose retraction are lost, leading to alleviation of T4P frustration (Fig. 5a). Finally, without T4P retraction (Δ*pilT*), no signal is produced even in the presence of mannose/Psl and CdrA (Fig. 5d). Cells can remain attached to the surface by their CdrA–mannose/Psl binding but are unable to retract T4P to twitch (Figs. 3a,c and 5d). Without the ability to initiate retraction, thus also losing any possibility of T4P frustration, there is neither cAMP nor cdGMP expression. This illustrates T4P retraction and cAMP generation being prerequisites for the resistance required for cdGMP generation at a population scale, which is consistent with previous work that suggests that cAMP signalling can precede cdGMP signalling in some circumstances[11].

Many species are known to use EPS in biofilm formation on surfaces, although how EPS in turn influences bacterial surface behaviour is largely unknown. While previous works have shown cdGMP dependence on Psl and CdrA binding to Psl (refs. 18,30), the connection between Psl–adhesin binding and Psl-mediated intracellular signalling remains unclear. Previous studies have also shown that Pa are capable of sensing shear stresses on a surface in a T4P-dependent manner[43]. However, these effects are not related to specific EPS, and no mechanism has been proposed. Our work serves to integrate previous observations and to show a mechanism whereby cells are capable of chemosensing using mechanosensing, rather than the traditional signal transduction mechanisms such as two-component systems. We have shown that surface-associated EPS sensing in Pa proceeds via a T4P-mediated force sensing of bonds between saccharide motifs (for example, mannose) and saccharide-specific adhesins (for example, CdrA) during retraction. This results in an outside-in transduction of EPS signalling through T4P to intracellular second messenger signals, cognate to surface sensing. This process creates a non-canonical subpopulation of trail-following bacteria with elevated cdGMP and elevated cAMP and high motility, a distinct state of biofilm development intermediate between free-swimming planktonic and fully biofilm-committed cells. This efficient saccharide detection framework builds on existing surface sensing circuits, which generate oscillatory second messenger signals that allow for high information density[26]. This makes the system generalizable and multiplexable without the need for separate saccharide sensing and transduction machinery, as T4P can potentially be used to detect other adhesin–saccharide interactions.

Methods

Strains and growth conditions

P. aeruginosa strain PAO1 WT[30] was used as the genetic background for mutants in this study, which were the markerless deletion of *cdrA* (Δ*cdrA*)[44]; markerless deletion of *pslB*, *pslC* and *pslD* (Δ*pslBCD*)[30]; and markerless deletion of *pilT* (Δ*pilT*). All strains contained the pBBR1MCS5-Ppaqa-mScarlet-I(ASV)-tet2-PcdrA-mGL(ASV)-t0t1-PrpoD-SCFP3A(ASV) reporter plasmid[21]. Modified fastidious anaerobe broth (FAB) medium[45] with 0.6 mM glutamate (Sigma-Aldrich) as the carbon source was used for flow cell experiments. An inoculum for flow cell imaging was prepared by growing strains containing FAB medium with 30 mM glutamate, supplemented with 100 μg ml^{-1} gentamicin

(Sigma-Aldrich) when appropriate. Cultures were serially diluted to 10^{-4} initial cell concentration before being grown overnight in test tubes, at 37 °C and shaking at 220 rpm, to mid-exponential phase, an optical density at 600 nm (OD_{600nm}) ~0.4 A. Cultures were then diluted to OD_{600nm} ~0.01 A in FAB medium with 0.6 mM glutamate, which was then used for injection into the flow cell system.

Polymannose synthesis and characterization

With the use of the following protocol, 2-*O*-(α-D-mannosyl)hydroxyethyl acrylate and poly-2-*O*-(α-D-mannosyl)hydroxyethyl acrylate (polymannose) were synthesized[22]. Lyophilization was conducted on a FreeZone 4.5-l benchtop freeze-dryer (Labconco). With an Avance-300 spectrometer (Bruker), ^{1}H NMR spectra were acquired. Glycopolymer samples were dissolved in D_2O and scanned in a 300-MHz magnetic field.

Materials. D-Mannose (Amresco, high purity grade), acetic anhydride (Fisher, American Chemical Society (ACS) grade), boron trifluoride etherate (ACROS, 48%), sodium methoxide in methanol (ACROS, 5.4 M), methanol (EMD DriSolv, 99.8%), ethanol (Decon Labs, 200 proof), ethyl acetate (Fisher, ACS grade), hexanes (Fisher, ACS grade), DOWEX 50WX8 ion-exchange resin (ACROS, 200–400 mesh) and 4-cyano-4-(thiobenzoylthio)pentanoic acid (Sigma-Aldrich) were used as received. Cyanovaleric acid (Pfalz and Bauer, 98%) was recrystallized from methanol. Hydroxyethyl acrylate (Sigma-Aldrich, 96%), dichloromethane (DCM, Fisher, ACS grade), pyridine (JT Baker, ACS grade) and water (Fisher, HPLC) were distilled for polymer synthesis procedures.

2-*O*-(α-D-Mannosyl)hydroxyethyl acrylate. For 1,2,3,4,6-pentaacetyl-α,β-D-mannose, acetic anhydride (50 ml, 0.53 mol) was added to a solution of D-mannose (10.0445 g, 55 mmol) dissolved in pyridine (100 ml) and the solution was stirred for 24 h. The solution was concentrated in vacuo and added to cold deionized (DI) water (450 ml). The product was taken up in DCM and washed with a saturated sodium bicarbonate solution (2 × 50 ml), washed with brine, dried with sodium sulfate and concentrated in vacuo. Trace pyridine was removed by dissolving in DCM and washing with 0.1 M aq. HCl (2 × 25 ml), drying over Na_2SO_4 and concentrating (5.0251 g, 23%). ^{1}H NMR (300 MHz, $CDCl_3$): δ 6.10 (d, H-1α), 5.89 (d, H-1β), 5.10–5.50 (m, H-2,3,4), 3.71–4.30 (m, H-5α, H2-6), 3.83 (m, H-5β), 2.00–2.19 (s, 15H, 5 CH_3).

2-*O*-(2,3,4,6-Tetraacetyl-α-D-mannosyl)hydroxyethyl acrylate. Boron trifluoride etherate (2.7 ml, 14 mmol) was added dropwise to a stirring solution of 1,2,3,4,6-pentaacetyl-α,β-D-mannose (3.24 g, 8.3 mmol) and hydroxyethyl acrylate (1.0 ml, 8.7 mmol) dissolved in DCM (25 ml) cooled in an ice bath. The solution was allowed to warm to room temperature after the addition was completed and stirred for 96 h. The reaction was washed with DI water (3 × 20 ml), a saturated solution of sodium bicarbonate (3 × 15 ml) and brine. The organic solution was dried with sodium sulfate, concentrated and isolated by silica column chromatography using 11:9 ethyl acetate in hexanes as an eluent (1.0599 g, 29%). ^{1}H NMR (300 MHz, $CDCl_3$): δ 6.43 (d, 1H, CH_2=CH), 6.15 (m, CH_2=CH), 5.87 (d, 1H, CH_2=CH), 5.20–5.40 (m, H-2,3,4), 4.87 (d, H-1), 4.34 (m, 2H, OCH_2CH_2OC=O), 4.03–4.27 (m, 3H, H-5, H2-6), 3.78–3.90 (m, 2H, OCH_2CH_2OC=O), 1.99–2.17 (s, 12H, 4 CH_3).

2-*O*-(α-D-Mannosyl)hydroxyethyl acrylate. Sodium methoxide in MeOH (37 µl, 0.2 mmol, 5.4 M) was added to a solution of 2-*O*-(2,3,4,6-tetraacetyl-α-D-mannosyl)hydroxyethyl acrylate (1.0599 g, 3.3 mmol) dissolved in DCM (5 ml) and methanol (4 ml), and the solution was stirred for 3 min before quenching with DOWEX 50WX8 ion-exchange resin for 15 min. The glycomonomer was isolated by silica column chromatography using 2:8 methanol in DCM as an eluent (228 mg, 24.7%). ^{1}H NMR (300 MHz, MeOD): δ 6.40 (d, 1H, CH_2=CH), 6.19 (m, CH_2=CH), 5.90 (d, 1H, CH_2=CH), 4.80 (d, H-1), 4.34 (m, 2H, OCH_2CH_2OC=O), 3.94 (m, 1H, OCH_2CH_2OC=O), 3.58–3.81 (m, 7H, H-2,3,4,5, H2-6, OCH_2CH_2OC=O).

Reversible addition–fragmentation chain transfer polymerization. Three stock solutions were made: 228 mg 2-*O*-(α-D-mannosyl) hydroxyethyl acrylate in 3 ml H_2O (monomer stock), 12.2 mg 4-cyano-4-(thiobenzoylthio)pentanoic acid in 2 ml EtOH (CTA stock) and 7.3 mg cyanovaleric acid in 4 ml EtOH (azo stock). Then, 1.5 ml monomer stock (114 mg, 0.41 mmol, 75 eq), 250 µl CTA stock (1.525 mg, 0.0055 mmol, 1 eq) and 250 µl azo stock (0.456 mg, 0.0016 mmol, 0.3 eq) were combined in a Schlenk flask (overall 3:1 water-to-ethanol ratio, 2 ml total volume). The solution was degassed by eight freeze–pump–thaw cycles and heated at 70 °C for 93 h followed by quenching in liquid nitrogen and exposure to air. The samples were diluted in H_2O and lyophilized, and triturated with warm ethanol to remove unreacted monomer. The resultant polymer was analysed by ^{1}H NMR and gel permeation chromatography. ^{1}H NMR was performed to characterize the spectrum for polymannose with the phenyldithocarbonate chain end intact (Extended Data Fig. 1). Using this chain end, we calculate the degree of polymerization to be 79 (chain end integration (A–C) = (0.02 + 0.01 + 0.03)/5 = 0.012 per H; repeat unit integration (E–I) (1.89 + 7.75 + 1.00 + 1.87) = 12.26/13 = 0.943 per H; DPn = 0.943/0.012 = 79). Gel permeation chromatography was conducted on a Jasco system equipped with a UV detector, a refractive index detector and four Waters ultrahydrogel columns (100–5,000, 1,000–80,000, 10,000–400,000, 2,000–4,000,000, 500–10,000,000) using water as an eluent at 30 °C and a flow rate of 1.0 ml min^{-1} calibrated using pullulan standards. While this method does not provide an accurate molecular weight (which is instead obtained from ^{1}H NMR), it indicates a polydispersity of 1.12, somewhat narrower than the polydispersity obtained for polymannose previously[22].

Glycopolymer patterning

Glass coverslips (number 1.5, Marienfeld-Superior) were patterned with a series of 4-µm-width lines with a periodicity of 15 µm in the following manner[22]. Samples were cleaned using piranha etch solution before baking at 150 °C for 10 min for dehydration. They were then exposed to hexamethyldisilazane vapours for 10 min to promote adhesion. AZ nLOF 2020 negative tone photoresist was deposited onto the coverslips and spin coated at 500 rpm for 5 s and then 3,000 rpm for 30 s. Coverslips were then soft-baked for 1 min at 110 °C. Total exposure on a Karl Suss contact aligner was 27.6 mJ. Post-exposure bake was performed for 1 min at 110 °C. The coverslips were then descummed with oxygen plasma at 100 °C for 3 min. Subsequently, 2 nm of titanium and 2 nm of gold were deposited onto the coverslip surface by a Solution E-beam Evaporator (CHA Industries). The photoresist was removed using PRS-3000 (J.T. Baker) photoresist stripper composed of approximately 50% 1-methyl-2-pyrrolidinone, 40% tetrahydrothiophene 1,1-dioxide and 1-amino-2-propanol. The samples were left in the photoresist stripper overnight at room temperature or for 1 h at 60 °C. The coverslips were then rinsed three times with DI water and dried with HEPA-filtered air. Final pattern dimensions were 4.8 ± 0.2 µm in width and a periodicity of 14.1 ± 0.3 µm. Alignment markers of equal width and length were included in the pattern for drift correction during imaging.

Patterned glass coverslips were then assembled into flow cells using Sticky-Slide $VI^{0.4}$ (ibidi) flow cells. For self-assembly, glycopolymers were dissolved in ultrapure water at a concentration of 3 mg ml^{-1}. A total of 100 µl of ethanolamine was added to the glycopolymer solution per 1 ml of water to cleave the disulfide bonds. Then, 50 µl of the glycopolymer solution was aliquoted into each patterned flow cell channel and self-assembly was allowed to proceed for 3 days at room temperature. The solution was then removed and flow cell channels washed with ultrapure water before sterilization and use.

Flow cell experiments

The patterned flow cells were then connected to a syringe through a 0.22-µm filter (Fisher Scientific) using a Silastic silicone tubing of inner diameter 1.57 mm and outer diameter 3.18 mm (Dow Corning) and a natural Kynar poly(vinylidene difluoride) (PVDF) female Luer to 1.6-mm barb adaptor (Value Plastics DBA Nordson Medical). An in-line injection port (ibidi) was used at the inlet for inoculating bacteria into the flow cell. Elbow connectors (ibidi) were used to connect the chamber with tubing. The assembled system was flushed with 70% ethanol at a volumetric flow rate of 25 ml h^{-1} using a syringe pump (KD Scientific or Harvard Apparatus) before being flushed with autoclaved, DI water at a flow rate of 5 ml h^{-1} using a syringe pump and allowed to sit overnight. Before the inoculation of the bacteria into the flow cell, the flow cell system was flushed with 5 ml of flow cell medium at 30 ml h^{-1}. The diluted bacterial culture was injected into the flow cell and allowed to incubate for 20 min without flow on the heating stage at 30 °C to promote surface attachment. Flow was then started at 3 ml h^{-1} for the entire acquisition time[12,13,25,26].

Data acquisition

Images were acquired using an Orca Quest quantitative complementary metal-oxide-semiconductor (qCMOS) camera (Hamamatsu Photonics) with Micro-Manager (v2.0.0)[46,47] on an Olympus IX83 microscope equipped with a Zero Drift Compensation (ZDC2) continuous autofocus system, with a ×100 oil-immersion objective (NA = 1.40) using 2 × 2 binning. Bright-field images were acquired at 1 Hz frequency (5 ms exposure time). For fluorescent images, images were taken every 5 min (50-ms exposure time) using an X-Cite XYLIS LED illumination system (Excelitas Technologies) at 10% power and a TexasRed, GFP and CFP filter for the mScarlet-I, mGreenLantern and SCFP3A fluorophores, respectively. This fluorescence interval was optimized for minimal phototoxicity and photobleaching effects. The total acquisition time for each experiment was between ~24 h and 80 h depending on the mutant, resulting in up to 300,000 bright-field images and 1,000 fluorescence images for each fluorophore channel per experiment. The image size was 188 µm × 106 µm (2,048 × 1,152 pixels, 0.092 µm per pixel) at 2 × 2 binning.

Image and data analysis

Image and data analyses were performed as follows. The image segmentation routine used Julia (v1.10 and v1.11)[48], with the Images (v0.25 and v0.26)[49] and MAT (v0.10)[50] packages. Before image segmentation, bright-field images were drift corrected using the RegisterQD (v0.3)[51] package, background and pattern subtracted, and passed through a Laplacian of Gaussian filter. Segmentation was performed using Otsu's method from the HistogramThresholding (v0.3)[52] package, which was the same method previously used in the MATLAB routine. MATLAB functions from the base installation of MATLAB R2015a, Statistics and Machine Learning Toolbox, Curve Fitting Toolbox, Image Processing Toolbox, Signal Processing Toolbox (all toolboxes come from the R2015a version), and custom MATLAB functions were used for tracking without modification from previous work[12,13,25,26]. This tracking routine processed segmented images with a sequence of algorithms using maximum bacteria feature overlap (binary image connected components) and minimum displacement (Hungarian algorithm) between consecutive frames and history-based segmentation of neighbouring cells, and then linked cells in different frames in time. All post-tracking analysis was performed in Julia (v1.10 and v1.11)[48], with the plots generated using Pluto (v0.20)[53] notebooks and Makie/CairoMakie (v0.12)[54] packages. No experimental data were excluded from the analysis before tracking. Cells that stayed on the surface for less than the fluorescence interval (5 min) were excluded from subsequent analyses after tracking owing to insufficient fluorescence reporter information. Post-tracking analysis was agnostic to experiment sample identity. Extraction of cAMP and cdGMP reporter signals was performed by first background subtracting each fluorescence image (by fitting a Gaussian to the intensity distribution and then taking the 3-sigma value of that distribution as the background value) and then dividing the corresponding reporter image by the normalizer image. The tracking output was used to determine the regions of the surface containing secreted trails. For each analysed time point, only cells that had stayed on the surface for at least 5 min previously were used, and the secreted trail region was constructed by taking the union of all these cells' segmentation masks. Determining whether a cell is twitching was performed by using the surface translational motility metric[12], which uses mean squared displacement (MSD) slope and cell displacement.

Statistics

Data and statistical analyses were performed in Julia (v1.10 and v1.11)[48], using the Bootstrap (v2.4)[55], CSV (v0.10)[56], DataFrames (v1.7)[57], HypothesisTests (v0.11)[58], KernelDensity (v0.6)[59], PolygonOps (v0.1)[60], Random (v1.11)[48], Statistics (v1.11)[48] and StatsBase (v0.34)[61] packages. All comparisons made were done using a two-sided Mann–Whitney *U* test (Wilcoxon rank-sum test) with Bonferroni multiple test correction (no star, $P \geq 0.05$; $^{*}P < 0.05$, $^{**}P < 0.001$). Error bars and exact comparisons used in each panel are described in their corresponding figure captions. Calculations to predetermine sample size were not performed, as sample size was determined automatically by the data processing and analysis pipeline as the number of tracked cells in each flow cell experiment. Each flow cell experiment is a biological replicate. In each experiment, each tracked cell can be considered a technical replicate. For the WT, 4 biological replicates were performed on patterned surfaces and 3 biological replicates on unpatterned surfaces, and for each mutant, 4 biological replicates were performed on patterned surfaces. For each biological replicate, the starting numbers of tracked cells before aggregating were as follows: WT patterned (n = 28,882, 23,445, 18,052, 10,724), Δ*cdrA* (n = 20,490, 21,009, 18,011, 25,885), Δ*pslBCD* (n = 17,455, 17,350, 16,703, 20,977), Δ*pilT* (n = 15,967, 18,495, 15,720, 14,009) and WT unpatterned (n = 12,459, 16,344, 15,615).

Reporting summary

Further information on research design is available in the Nature Portfolio Reporting Summary linked to this article.

Data availability

Data used to generate the plots in the figures are available via Figshare at https://doi.org/10.6084/m9.figshare.29367470 (ref. 62) and via Zenodo at https://doi.org/10.5281/zenodo.15777167 (ref. 63). Additional experimental data are available upon request.

Code availability

Code used to generate the plots in the figures are available via Figshare at https://doi.org/10.6084/m9.figshare.29367470 (ref. 62) and via Zenodo at https://doi.org/10.5281/zenodo.15777167 (ref. 63). The code and data are an integrated package uploaded to the same location, and running the code will automatically load the data with its current folder hierarchy.

References

1. Moreau-Marquis, S., Stanton, B. A. & O'Toole, G. A. *Pseudomonas aeruginosa* biofilm formation in the cystic fibrosis airway. *Pulm. Pharmacol. Ther.* **21**, 595–599 (2008).
2. Whitchurch, C. B., Tolker-Nielsen, T., Ragas, P. C. & Mattick, J. S. Extracellular DNA required for bacterial biofilm formation. *Science* **295**, 1487–1487 (2002).
3. Flemming, H.-C. & Wingender, J. The biofilm matrix. *Nat. Rev. Microbiol.* **8**, 623–633 (2010).

4. Ma, L., Wang, S., Wang, D., Parsek, M. R. & Wozniak, D. J. The roles of biofilm matrix polysaccharide Psl in mucoid *Pseudomonas aeruginosa* biofilms. *FEMS Immunol. Med. Microbiol.* **65**, 377–380 (2012).
5. Ryder, C., Byrd, M. & Wozniak, D. J. Role of polysaccharides in *Pseudomonas aeruginosa* biofilm development. *Curr. Opin. Microbiol.* **10**, 644–648 (2007).
6. Ma, L., Lu, H., Sprinkle, A., Parsek, M. R. & Wozniak, D. J. *Pseudomonas aeruginosa* Psl is a galactose- and mannose-rich exopolysaccharide. *J. Bacteriol.* **189**, 8353–8356 (2007).
7. Byrd, M. S. et al. Genetic and biochemical analyses of the *Pseudomonas aeruginosa* Psl exopolysaccharide reveal overlapping roles for polysaccharide synthesis enzymes in Psl and LPS production. *Mol. Microbiol.* **73**, 622–638 (2009).
8. Hickman, J. W., Tifrea, D. F. & Harwood, C. S. A chemosensory system that regulates biofilm formation through modulation of cyclic diguanylate levels. *Proc. Natl Acad. Sci. USA* **102**, 14422–14427 (2005).
9. Hickman, J. W. & Harwood, C. S. Identification of FleQ from *Pseudomonas aeruginosa* as a c-di-GMP-responsive transcription factor. *Mol. Microbiol.* **69**, 376–389 (2008).
10. Baraquet, C., Murakami, K., Parsek, M. R. & Harwood, C. S. The FleQ protein from *Pseudomonas aeruginosa* functions as both a repressor and an activator to control gene expression from the pel operon promoter in response to c-di-GMP. *Nucleic Acids Res.* **40**, 7207–7218 (2012).
11. Luo, Y. et al. A hierarchical cascade of second messengers regulates *Pseudomonas aeruginosa* surface behaviors. *mBio* **6**, e02456-14 (2015).
12. Lee, C. K. et al. Multigenerational memory and adaptive adhesion in early bacterial biofilm communities. *Proc. Natl Acad. Sci. USA* **115**, 4471–4476 (2018).
13. Lee, C. K. et al. Social cooperativity of bacteria during reversible surface attachment in young biofilms: a quantitative comparison of *Pseudomonas aeruginosa* PA14 and PAO1. *mBio* **11**, e02644-19 (2020).
14. Whitchurch, C. B., Hobbs, M., Livingston, S. P., Krishnapillai, V. & Mattick, J. S. Characterisation of a *Pseudomonas aeruginosa* twitching motility gene and evidence for a specialised protein export system widespread in eubacteria. *Gene* **101**, 33–44 (1991).
15. Burrows, L. L. *Pseudomonas aeruginosa* twitching motility: type IV pili in action. *Annu. Rev. Microbiol.* **66**, 493–520 (2012).
16. Persat, A., Inclan, Y. F., Engel, J. N., Stone, H. A. & Gitai, Z. Type IV pili mechanochemically regulate virulence factors in *Pseudomonas aeruginosa*. *Proc. Natl Acad. Sci. USA* **112**, 7563–7568 (2015).
17. Zhao, K. et al. Psl trails guide exploration and microcolony formation in *Pseudomonas aeruginosa* biofilms. *Nature* **497**, 388–391 (2013).
18. Irie, Y. et al. Self-produced exopolysaccharide is a signal that stimulates biofilm formation in *Pseudomonas aeruginosa*. *Proc. Natl Acad. Sci. USA* **109**, 20632–20636 (2012).
19. Sanchez, H., O'Toole, G. A. & Berwin, B. Assessment of the glycan-binding profile of *Pseudomonas aeruginosa* PAO1. *Microbiol. Spectr.* **11**, e01667 (2023).
20. Bar-Shavit, Z., Ofek, I., Goldman, R., Mirelman, D. & Sharon, N. Mannose residues on phagocytes as receptors for the attachment of *Escherichia coli* and *Salmonella typhi*. *Biochem. Biophys. Res. Commun.* **78**, 455–460 (1977).
21. Zheng, X. et al. The surface interface and swimming motility influence surface-sensing responses in *Pseudomonas aeruginosa*. *Proc. Natl Acad. Sci. USA* **121**, e2411981121 (2024).
22. Young, T. D. et al. Selective promotion of adhesion of *Shewanella oneidensis* on mannose-decorated glycopolymer surfaces. *ACS Appl. Mater. Interfaces* **12**, 35767–35781 (2020).
23. Simm, R., Morr, M., Kader, A., Nimtz, M. & Römling, U. GGDEF and EAL domains inversely regulate cyclic di-GMP levels and transition from sessility to motility. *Mol. Microbiol.* **53**, 1123–1134 (2004).
24. Römling, U. & Amikam, D. Cyclic di-GMP as a second messenger. *Curr. Opin. Microbiol.* **9**, 218–228 (2006).
25. Armbruster, C. R. et al. Heterogeneity in surface sensing suggests a division of labor in *Pseudomonas aeruginosa* populations. *eLife* **8**, e45084 (2019).
26. Lee, C. K. et al. Broadcasting of amplitude- and frequency-modulated c-di-GMP signals facilitates cooperative surface commitment in bacterial lineages. *Proc. Natl Acad. Sci. USA* **119**, e2112226119 (2022).
27. Gibiansky, M. L., Hu, W., Dahmen, K., Shi, W. & Wong, G. C. L. Earthquake-like dynamics in *Myxococcus xanthus* social motility. *Proc. Natl Acad. Sci. USA* **110**, 2330–2335 (2013).
28. Hu, W. et al. Interplay between type IV pili activity and exopolysaccharides secretion controls motility patterns in single cells of *Myxococcus xanthus*. *Sci. Rep.* **6**, 17790 (2016).
29. Cooley, R. B. et al. Cyclic di-GMP-regulated periplasmic proteolysis of a *Pseudomonas aeruginosa* type Vb secretion system substrate. *J. Bacteriol.* **198**, 66–76 (2016).
30. Borlee, B. R. et al. *Pseudomonas aeruginosa* uses a cyclic-di-GMP-regulated adhesin to reinforce the biofilm extracellular matrix. *Mol. Microbiol.* **75**, 827–842 (2010).
31. Reichhardt, C. et al. The versatile *Pseudomonas aeruginosa* biofilm matrix protein CdrA promotes aggregation through different extracellular exopolysaccharide interactions. *J. Bacteriol.* **202**, e00216–e00220 (2020).
32. Melia, C. E. et al. Architecture of cell–cell junctions in situ reveals a mechanism for bacterial biofilm inhibition. *Proc. Natl Acad. Sci. USA* **118**, e2109940118 (2021).
33. Geiger, C. J. & O'Toole, G. A. Evidence for the type IV pilus retraction motor PilT as a component of the surface sensing system in *Pseudomonas aeruginosa*. *J. Bacteriol.* **205**, e0017923 (2023).
34. Utada, A. S. et al. *Vibrio cholerae* use pili and flagella synergistically to effect motility switching and conditional surface attachment. *Nat. Commun.* **5**, 4913 (2014).
35. Yarrington, K. D., Shendruk, T. N. & Limoli, D. H. The type IV pilus chemoreceptor PilJ controls chemotaxis of one bacterial species towards another. *PLoS Biol.* **22**, e3002488 (2024).
36. Webster, S. S. et al. Force-induced changes of PilY1 drive surface sensing by *Pseudomonas aeruginosa*. *mBio* **13**, e0375421 (2022).
37. Webster, S. S., Wong, G. C. L. & O'Toole, G. A. The power of touch: type 4 pili, the von Willebrand A domain, and surface sensing by *Pseudomonas aeruginosa*. *J. Bacteriol.* **204**, e0008422 (2022).
38. Dufrêne, Y. F. & Persat, A. Mechanomicrobiology: how bacteria sense and respond to forces. *Nat. Rev. Microbiol.* **18**, 227–240 (2020).
39. Beaussart, A. et al. Nanoscale adhesion forces of *Pseudomonas aeruginosa* type IV pili. *ACS Nano* **8**, 10723–10733 (2014).
40. Ribbe, J., Baker, A. E., Euler, S., O'Toole, G. A. & Maier, B. Role of cyclic di-GMP and exopolysaccharide in type IV pilus dynamics. *J. Bacteriol.* **199**, e00859-16 (2017).
41. Beaussart, A. et al. Atomic force microscopy analysis of Pel polysaccharide- and type IV pili-mediated adhesion of *Pseudomonas aeruginosa* PA14 to an abiotic surface. *Nanoscale* **16**, 12134–12141 (2024).
42. Talà, L., Fineberg, A., Kukura, P. & Persat, A. *Pseudomonas aeruginosa* orchestrates twitching motility by sequential control of type IV pili movements. *Nat. Microbiol.* **4**, 774–780 (2019).
43. Rodesney, C. A. et al. Mechanosensing of shear by *Pseudomonas aeruginosa* leads to increased levels of the cyclic-di-GMP signal initiating biofilm development. *Proc. Natl Acad. Sci. USA* **114**, 5906–5911 (2017).

44. Reichhardt, C., Wong, C., Passos da Silva, D., Wozniak, D. J. & Parsek, M. R. CdrA interactions within the *Pseudomonas aeruginosa* biofilm matrix safeguard it from proteolysis and promote cellular packing. *mBio* **9**, e01376-18 (2018).
45. Heydorn, A. et al. Quantification of biofilm structures by the novel computer program COMSTAT. *Microbiology* **146**, 2395–2407 (2000).
46. Edelstein, A., Amodaj, N., Hoover, K., Vale, R. & Stuurman, N. Computer control of microscopes using μManager. *Curr. Protoc. Mol. Biol.* **92**, 14.20.1–14.20.17 (2010).
47. Edelstein, A. D. et al. Advanced methods of microscope control using μManager software. *J. Biol. Methods* **1**, e10 (2014).
48. Bezanson, J., Edelman, A., Karpinski, S. & Shah, V. B. Julia: a fresh approach to numerical computing. *SIAM Rev.* **59**, 65–98 (2017).
49. JuliaImages/Images.jl (JuliaImages, 2024).
50. JuliaIO/MAT.jl (JuliaIO, 2024).
51. Holy, T. HolyLab/RegisterQD.jl (Holy Lab, 2023).
52. JuliaImages/HistogramThresholding.jl (JuliaImages, 2021).
53. Plas van der, F. et al. fonsp/Pluto.jl: v0.20.0. Zenodo https://doi.org/10.5281/zenodo.13929878 (2024).
54. Danisch, S. & Krumbiegel, J. Makie.jl: flexible high-performance data visualization for Julia. *J. Open Source Softw.* **6**, 3349 (2021).
55. Gehring, J. et al. juliangehring/Bootstrap.jl: Bootstrap v2.4.0. Zenodo https://doi.org/10.5281/zenodo.10073439 (2023).
56. Quinn, J. et al. JuliaData/CSV.jl: v0.10.15. Zenodo https://doi.org/10.5281/zenodo.13955982 (2024).
57. Bouchet-Valat, M. & Kamiński, B. DataFrames.jl: flexible and fast tabular data in Julia. *J. Stat. Softw.* **107**, 1–32 (2023).
58. JuliaStats/HypothesisTests.jl (Julia Statistics, 2024).
59. JuliaStats/KernelDensity.jl (Julia Statistics, 2024).
60. JuliaGeometry/PolygonOps.jl (JuliaGeometry, 2020).
61. JuliaStats/StatsBase.jl (Julia Statistics, 2024).
62. Lee, C. K. & Schmidt, W. C. Data for "*Pseudomonas aeruginosa* senses exopolysaccharide trails using type IV pili and adhesins during biofilm formation". *figshare* https://doi.org/10.6084/m9.figshare.29367470 (2025).
63. Lee, C. K. & Schmidt, W. C. Data for "*Pseudomonas aeruginosa* senses exopolysaccharide trails using type IV pili and adhesins during biofilm formation". *Zenodo* https://doi.org/10.5281/zenodo.15777167 (2025).
64. Hanley, J. A. Receiver operating characteristic (ROC) methodology: the state of the art. *Crit. Rev. Diagn. Imaging* **29**, 307–335 (1989).

Acknowledgements

C.K.L., G.C.L.W. and M.R.P. are supported by the Army Research Office (W911NF-18-1-0254). W.C.S. is supported by the National Science Foundation (NSF) Graduate Research Fellowship (DGE-1650604, DGE-2034835) and by the National Institutes of Health (NIH) Ruth L. Kirschstein National Research Service Award 'Multidisciplinary Training in Microbial Pathogenesis' (NIH T32 AI007323). C.K.L., G.C.L.W. and G.A.O. are supported by the NIH (R01 AI143730). G.A.O. is also supported by the NIH (R37 AI083256). M.R.P. and X.Z. are supported by the NIH (R01 AI143916 and R01 AI077628). X.Z. is a Cystic Fibrosis Foundation Awardee of the Life Sciences Research Foundation. K.L.F. and J.R.P. are supported by NSF 1821721. J.W.C. is supported by the NIH Ruth L. Kirschstein National Research Service Award 'Systems in Integrative Biology' (NIH T32 GM008185). We thank B. Wi, S. Deng, W. Sun, E. Tseng, S. Perry, E. Nuño, B. Pang, A. Kang and A. Nguyen for their help with data collection and analysis. We also thank R. Archuleta, J. Dominguez, D. Estrada Castro, Z. Li, L. Yee and B. Zelaya for help with data collection through the Supporting Enrollment and Retention of Veterans in Engineering and Science (SERVES) programme at East Los Angeles College (ELAC) (NSF 1821721). We also acknowledge the California NanoSystems Institute (CNSI) Nanolab for the use of their facilities.

Author contributions

The project was conceived by G.C.L.W., M.R.P., G.A.O., A.M.K. and P.S.W. Experiments were designed by G.C.L.W., M.R.P., G.A.O., W.C.S., C.K.L. and X.Z. Bacterial strains were constructed by X.Z. and M.R.P. Glycopolymers were designed, synthesized and characterized by K.L.F., J.R.P. and A.M.K. Patterned surfaces were designed, fabricated and characterized by T.D.Y., W.C.S. and P.S.W. Experimental data were acquired by W.C.S., C.K.L. and Y.S.C. Image and data analyses were performed by C.K.L., W.C.S., J.W.C. and Y.S.C. Publication was prepared by W.C.S., C.K.L., G.C.L.W., G.A.O., M.R.P., K.L.F. and A.M.K. All authors discussed the results and commented on the paper.

Competing interests

The authors declare no competing interests.

Additional information

Extended data is available for this paper at https://doi.org/10.1038/s41564-025-02087-4.

Supplementary information The online version contains supplementary material available at https://doi.org/10.1038/s41564-025-02087-4.

Correspondence and requests for materials should be addressed to George A. O'Toole, Matthew R. Parsek or Gerard C. L. Wong.

Peer review information *Nature Microbiology* thanks Beiyan Nan and the other, anonymous, reviewer(s) for their contribution to the peer review of this work.

Reprints and permissions information is available at www.nature.com/reprints.

Publisher's note Springer Nature remains neutral with regard to jurisdictional claims in published maps and institutional affiliations.

Springer Nature or its licensor (e.g. a society or other partner) holds exclusive rights to this article under a publishing agreement with the author(s) or other rightsholder(s); author self-archiving of the accepted manuscript version of this article is solely governed by the terms of such publishing agreement and applicable law.

© The Author(s), under exclusive licence to Springer Nature Limited 2025

https://doi.org/10.1038/s41564-025-02087-4

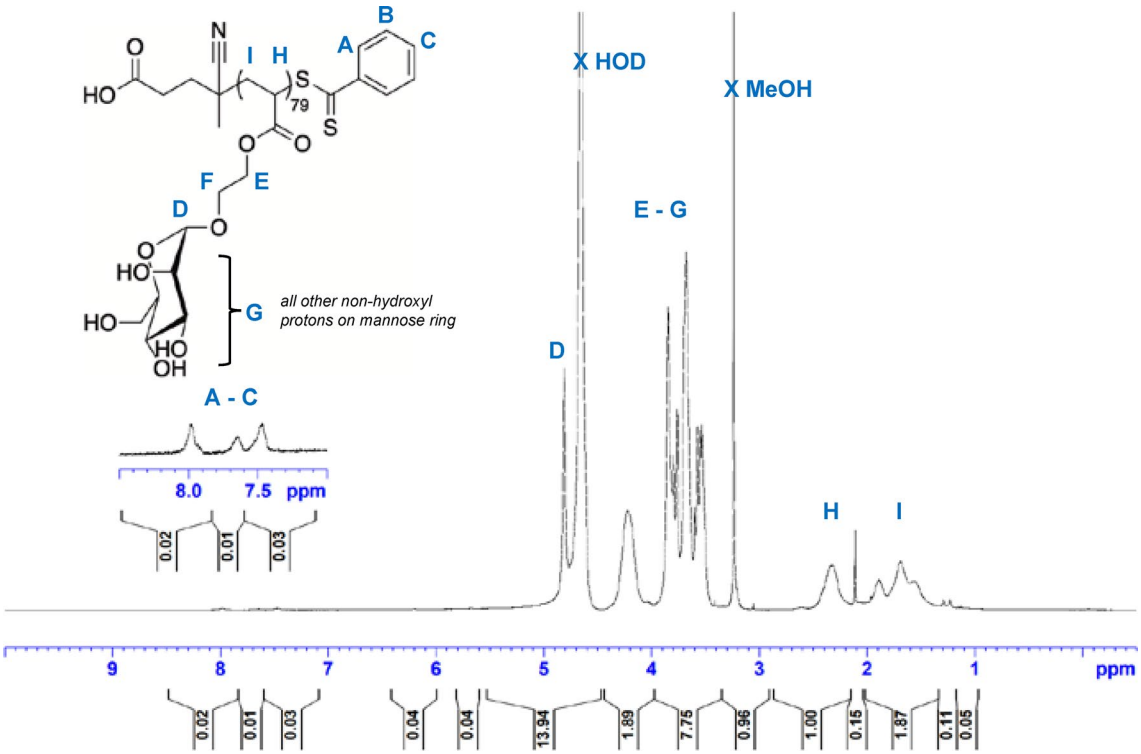

Extended Data Fig. 1 | Polymannose NMR Spectrum. ^{1}H NMR spectrum of polymannose in D_2O.

https://doi.org/10.1038/s41564-025-02087-4

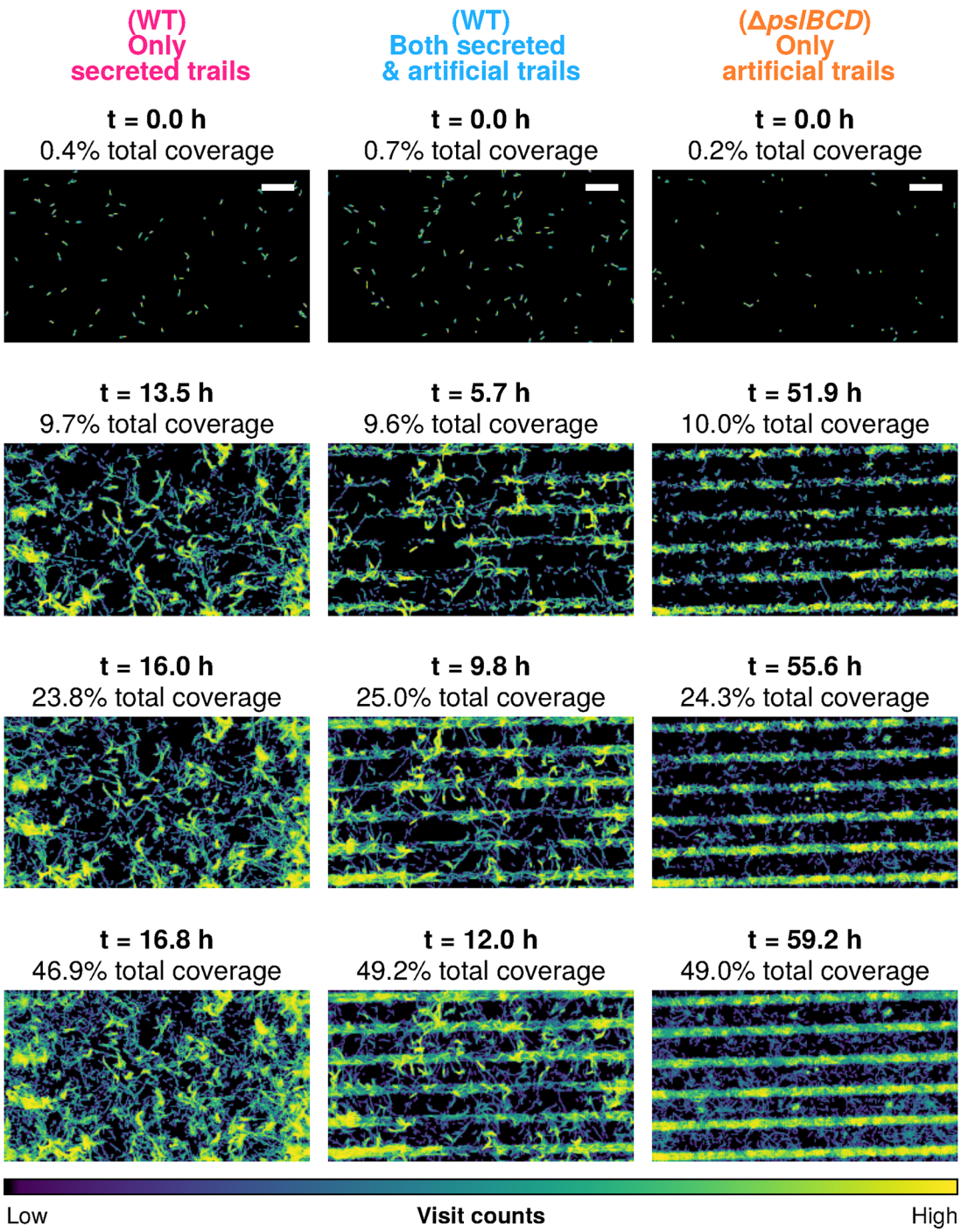

Extended Data Fig. 2 | Visit map montages on secreted and artificial trails. Visit map montages for the conditions in Fig. 1. Each column is one of the conditions, and each row is a different time point and total surface coverage value. The first row is just after inoculation (t = 0 h), and subsequent rows are the time points at 10%, 25%, and 50% total coverage. For comparison, the second row is the same as the visit maps displayed in Fig. 1. Scale bar 20 µm.

https://doi.org/10.1038/s41564-025-02087-4

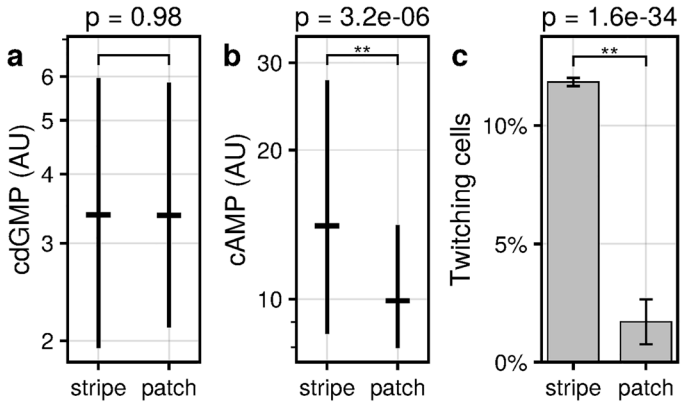

Extended Data Fig. 3 | The effect of artificial trail geometry on cell behavior. The effect of stripes vs patches of artificial EPS on (**a**) cdGMP signaling, (**b**) cAMP signaling, and (**c**) twitching motility for WT. Cells from all 4 biological replicates have been aggregated together and then subdivided into whether a cell is on a stripe or patch of artificial EPS. For (**a**) and (**b**), horizontal lines represent the median and the vertical whiskers represent the IQR of each subpopulation. For (**c**), bars and error bars represent the mean and standard deviation of the bootstrap sampling of each subpopulation mean twitching fraction, respectively. Cells on both stripes and patches have similar cdGMP levels, but cells on patches have lower cAMP levels and twitching fraction than cells on stripes. A two-sided Mann-Whitney U test with Bonferroni multiple test correction was used (no star $p \geq 0.05$; * $p < 0.05$; ** $p < 0.001$) for all comparisons (stripe vs patch). Adjusted p-values: (**a**) $p = 0.98$; (**b**) $p = 3.2 \times 10^{-6}$; (**c**) $p = 1.6 \times 10^{-34}$. Number of cells in each subpopulation: stripe, 40247; patch, 176. The starting numbers of cells per biological replicate before aggregating and subdividing: n = 28882, 23445, 18052, 10724.

https://doi.org/10.1038/s41564-025-02087-4

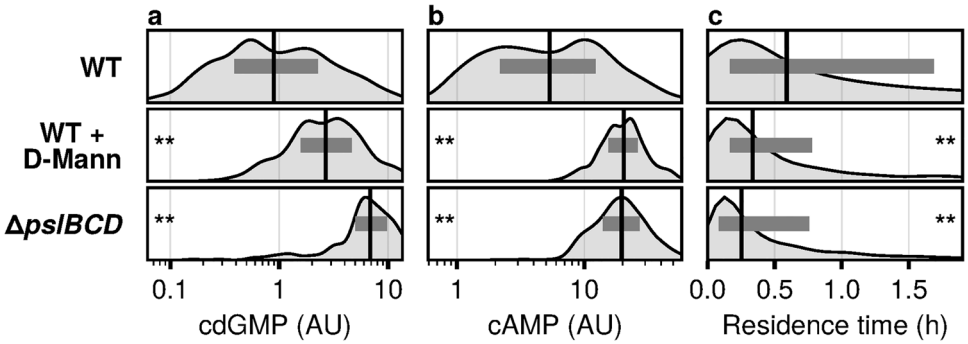

Extended Data Fig. 4 | Surface residence time with and without mannose. (**a**) cdGMP, (**b**) cAMP, and (**c**) residence time measurements for WT cells with and without non-metabolizable methyl-α-D-mannopyranoside (D-Mann) added exogenously to the media (20 mM) compared to cells lacking Psl production (Δ*pslBCD*), all on bare glass surfaces with no patterns. For each mutant, cells from all biological replicates have been aggregated together. Vertical lines represent the median and the whiskers represent the iqr of the population, and the probability distributions are calculated using kernel density estimates. A two-sided Mann-Whitney U test with Bonferroni multiple test correction was used (no star $p \geq 0.05$; * $p < 0.05$; ** $p < 0.001$) for all comparisons to WT without D-Mann. Adjusted p-values (top to bottom): (**a**) $p = 5 \times 10^{-185}$, 3×10^{-204}; (**b**) $p = 2.2 \times 10^{-16}$, 7.5×10^{-155}; (**c**) $p = 3.3 \times 10^{-12}$, 3.2×10^{-54}. The starting numbers of cells per biological replicate before aggregating: WT (n = 10334, 8149, 8995), WT D-Mann (n = 1245, 8, 1703), Δ*pslBCD* (n = 139, 28, 17461, 6536, 1344).

https://doi.org/10.1038/s41564-025-02087-4

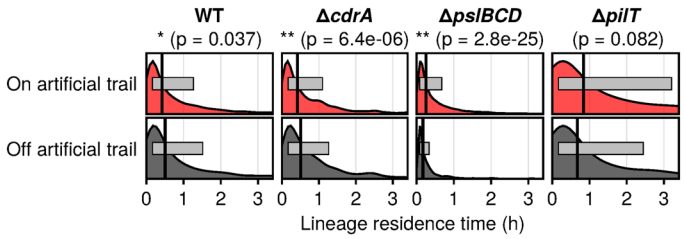

Extended Data Fig. 5 | Residence times for mutants. Residence time comparisons (using kernel density estimate) for the mutants in Fig. 3 *On* and *Off* of the artificial polymannose-patterned EPS trails. For each mutant, cells from all 4 biological replicates have been aggregated together and then subdivided accordingly. Vertical lines represent the median and the whiskers represent the IQR of each subpopulation, and the probability distributions are calculated using kernel density estimates. A two-sided Mann-Whitney U test with Bonferroni multiple test correction was used (no star $p \geq 0.05$; * $p < 0.05$; ** $p < 0.001$) for all comparisons of *on* vs *off* trail. Adjusted p-values (left to right): WT ($p = 0.037$); Δ*cdrA* ($p = 6.4 \times 10^{-6}$); Δ*pslBCD* ($p = 2.8 \times 10^{-25}$); Δ*pilT* ($p = 0.082$). Number of cells in each subpopulation: WT, 2936 *on* and 1258 *off*; Δ*cdrA*, 4202 *on* and 1516 *off*; Δ*pslBCD*, 9478 *on* and 872 *off*; Δ*pilT*, 1650 *on* and 736 *off*. The starting numbers of cells per biological replicate before aggregating and subdividing: WT (n = 28882, 23445, 18052, 10724), Δ*cdrA* (n = 20490, 21009, 18011, 25885), Δ*pslBCD* (n = 17455, 17350, 16703, 20977), Δ*pilT* (n = 15967, 18495, 15720, 14009).

https://doi.org/10.1038/s41564-025-02087-4

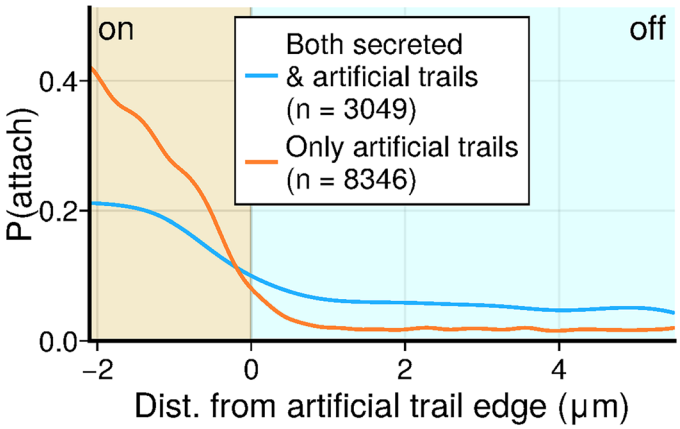

Extended Data Fig. 6 | Probability of cell attachment near pattern edges. Probability of cell attachment, using kernel density estimate, as a function of distance from pattern edge *on* (gold, negative values on the X-axis) or *off* (cyan, positive values on the X-axis) of the artificial polymannose trail. The number of attachment events used to calculate this probability was n = 3049 for both secreted and artificial trails and n = 8346 for only artificial trails, aggregated across all 4 biological replicates for each condition.

https://doi.org/10.1038/s41564-025-02087-4

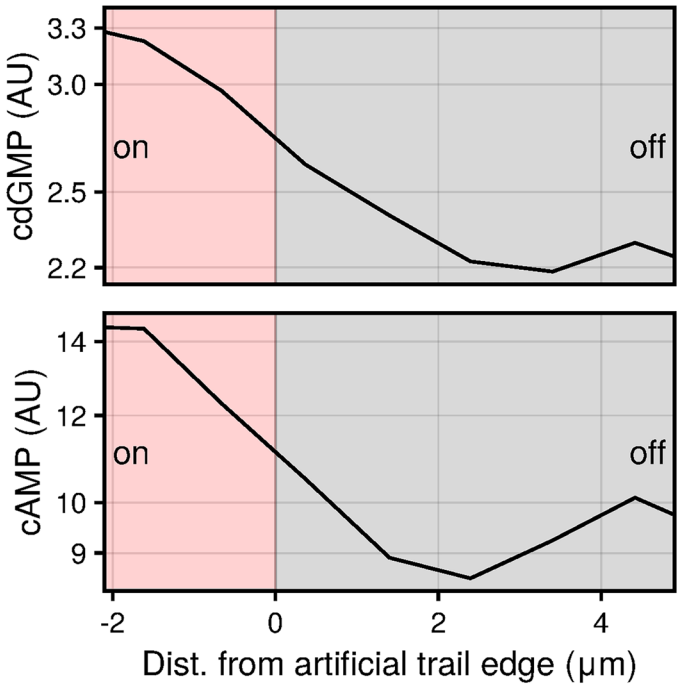

Extended Data Fig. 7 | Second messenger signaling near pattern edges. WT median cdGMP (top) and cAMP (bottom) expression as a function of cell distance from the artificial trail edge. Both cdGMP and cAMP are at their maximal level when cells are in the center of the artificial trail (red, negative X-axis), with expression dropping as location shifts towards the edge and *off* the artificial trail (grey, positive X-axis). Cells from all 4 biological replicates have been aggregated together and then subdivided by distance from the artificial trail edge. The starting numbers of cells per biological replicate before aggregating and subdividing: n = 28882, 23445, 18052, 10724.

nature microbiology

Supplementary information https://doi.org/10.1038/s41564-025-02087-4

Pseudomonas aeruginosa senses exopolysaccharide trails using type IV pili and adhesins during biofilm formation

In the format provided by the authors and unedited

Supplementary Discussion

Stereochemistry considerations for polymannose structure

In order to retain binding activity comparable to naturally produced polysaccharides, we modified the mannose monosaccharide at the anomeric position (C1). This modification best mimics the glycosidic linkage while retaining biological activity. Our synthetic approach favors the alpha-anomer.[65,66] While both *alpha* and *beta* glycosidic linkages are found in nature, *alpha*-linked mannose residues (e.g., α-(1→2), α-(1→3), α-(1→6)) are commonly found in oligo- and polysaccharide structures from non-mammalian sources.[67] For example, α-(1→2)-linked mannose oligosaccharides produced by *Mycobacterium tuberculosis* bind to Dectin-2, a C-type lectin.[68] In pathogenic *E. coli* strains, the fimbrial lectin FimH recognizes terminal mannose structures with α-(1→3)-linkages.[69] While the Psl oligosaccharide contains both *alpha* and *beta* mannose linkages,[7] previous studies have shown that PAO1 consistently and significantly binds α-d-mannose.[19]

Trail-induced cellular localization and trail-induced second messenger signaling depend on the distance between trail and cell body

By comparing cell attachment and signaling as a function of distance, we can determine the length scales associated with interactions with the artificial trails. Since EPS production is critical for *Pa* surface attachment,[41] we hypothesize that the Δ*pslBCD* mutant is entirely dependent on the artificial trails for surface attachment. This dependence is most apparent when attachment probability is quantified as a function of cell position relative to the artificial trail edge (ED Fig. 6). Attachment probability for the Δ*pslBCD* mutant is highest at the center of the artificial trail (-2 μm) and drops sharply to near zero *off* of the trail (+0.5 - 1.0 μm). WT exhibits a similar but softer trend, with the attachment probability plateauing at a non-zero value ~4× lower than the *on* trail maximum. These results highlight the importance of Psl in surface attachment and exploration. WT cells explore more of the surface through interacting with both artificial and secreted trails, but Δ*pslBCD* cells are restricted to only regions of the surface where artificial trails are present. When we compare cdGMP and cAMP signal expression in WT as a function of distance to the pattern edge (ED Fig 7), we find that, analogous to attachment probability, second messenger expression is also dependent on the location of the cell relative to the artificial trail. Both cdGMP and cAMP exhibit maximal expression at the center of the artificial trail (-2 μm) and drop to their minimum expression *off* of the trail (+1.5 - 2 μm). Interestingly, both cell attachment and signal expression begin to decrease while still *on* trail, as cells approach the edge. This result suggests the importance of physical contact between the cell body and trail for attachment and signaling, and, consequently, the trail preference observed in Fig 1d, e. The presence of secreted Psl trails allows for increased range of movement for cells onto and off of the artificial trails. In conjunction with the increase in twitching observed in relation to contact with artificial trails (Fig. 3c), this suggests that twitching plays a key role in establishing the gradient between *on* and *off* trail signal expression.

Geometry of artificial EPS trail strongly influences cellular surface behavior

Psl from *Pa* is primarily a linear polymer suited for maintaining adhesion to a surface.[7] This is in contrast to the EPS of other species, such as *Myxococcus xanthus*, which exhibit a highly branched EPS structure, a molecular architecture which in principle can mediate not only adhesion to the surface, but also in-plane lubricant-like behavior.[27] Consistent with this notion, the characteristic Social motility exhibited by *M. xanthus* exhibits strong motility correlations between cells and a slow (~50 - 100x slower than *Pa*) train-like motility on the surface, which appears smooth to the naked eye, but shows characteristic 'stick-slip' transitions in high speed microscopy.[28] However, the behavior of bacteria on EPS trails is not solely determined by the chemistry of the trails, as we observe enhanced motility on artificial trails in *Pa*. The geometry of the trail, specifically whether it is an EPS patch or a long, spatially extended EPS trail, exerts a strong influence on behavior. Given the same EPS chemical composition, spatially extended EPS trails generally enhance motility, whereas spatially localized EPS patches generally inhibit motility. Naturally secreted Psl trails are often sparse and patchy on the surface, leading to smaller areas for cellular interactions.[17] Artificial trails, because of their manufacturing, consist of more evenly distributed surface patterns, leading to a relative increase in the contact area for interaction.[22] The effect of this difference in pattern geometry on cell behavior is most exemplified through the introduction of isolated patches of artificial trails, which also serve as fiducial markers for the main striped pattern. While cells on the stripes have increased twitching, cells on the isolated markers exhibit more spatial confinement and, consequently, restricted twitching motility (ED Fig. 3), more similar to cells on isolated patches of Psl. These differences in twitching motility as a result of trail geometry likely contribute to consequent changes in cAMP exhibited between the natural Psl trails and the artificial polymannose trail.

T4P mechanisms for mediating cAMP and cdGMP second messenger signaling

There are a number of mechanisms that have been previously proposed that allow T4P to transduce external mechanical signals into second messenger signals that are consistent with the observations and model presented in this paper. While a strong correlation between cAMP and T4P biosynthesis has been established,[11,15] the exact connection between T4P-mediated twitching and cAMP expression remains less clear. There are several prevailing models for how T4P retraction can lead to cAMP production. Geiger et al. demonstrated that the retraction ATPase PilT interacts with PilJ, leading to an increase in cAMP via the Pil-Chp system.[11,33] PilU, the partner ATPase of PilT necessary for surface twitching also plays a role in mediating this cAMP expression, as overexpression of PilU results in decreased cAMP and vice versa.[33,42] An alternative model proposes PilA monomer as a signal for cAMP production, with increased retraction leading to internalization of more PilA monomer and thus increased cAMP expression.[16] Another model suggests that PilA interacts with PilJ but does not necessarily drive cAMP signaling.[70] Both of these force-dependent cAMP mechanosensing models would be consistent with the results and proposed model presented in this paper.

Like cAMP, cdGMP expression also has established mechanisms regulated by the T4P. T4P frustration represents the resistance encountered by the T4P during a retraction event, caused by cell body binding to the surface and thereby temporarily obstructing motility. This jittery motility behavior is characteristic of twitching motility, where T4P driven movement is 'stalled' or

frustrated until the collective adhesin binding on the cell body gives way.[27] In our system, the strength of cell-EPS interactions during this period of frustration can be sensed by the T4P, leading to the generation of second messenger signals in response. The prevailing model of how frustration of T4P retraction leads to cdGMP production is via a mechanosensing pathway composed of the T4P components PilY1 and PilO, and the DGC SadC.[37] In PA14, PilY1 is the tip protein of the T4P and has a von Willebrand A (vWA) mechanosensing domain that is capable of force-induced conformational change.[36] When the T4P are under tension, the vWA domain of PilY1 undergoes a sustained conformational change, which then can interact with PilO when the T4P tip is retracted. PilY1-PilO interactions then lead to the PilO-SadC signal transduction cascade, whereby PilO ceases interaction with SadC, allowing for the activation of the DGC, leading to cdGMP expression. Previous studies have shown that the measured binding force of the T4P to a surface can exceed the maximum retraction force of the PilT/PilU complex,[39,40] indicating the existence of a regime where T4P are under maximal tension but still incapable of retraction, where our proposed cdGMP mechanosensing would occur. Another potential connection between T4P mechanosensing and cdGMP expression is via FimX, a PDE that binds cdGMP with high affinity and is localized to the leading pole during twitching.[71,72] FimX is necessary for the PilB extension ATPase to function, through its cdGMP binding and also presumably PDE function.[73] Thus, in a condition in which PilT is unable to be unloaded due to frustrated T4P retraction, FimX PDE activity could be disrupted, which would consequently result in an increase in intracellular cdGMP. These two mechanisms of cdGMP expression are each congruent with our observations and proposed model and need not be mutually exclusive in generating a cdGMP response from T4P activity. It can also be possible for the T4P to serve multiple roles in cases where T4P are shown to exhibit binding to EPS directly, which has been reported in other species such as *M. xanthus*,[74] but has yet to be demonstrated in *Pa*.[39] Given the multi-piliated nature of *Pa*, the net cAMP and cdGMP expression profile of an individual cell could come from the combination of multiple T4P mechanosensing inputs, resulting in a spectrum of potential cAMP and cdGMP signal output depending upon the exact environmental conditions encountered by the cell.

Deposited EPS facilitates new surface attachment upon contact

Previous publications have shown that both T4P and EPS are required for attachment during cell contact with a surface. Tala et al. demonstrated that T4P employ a “catch bond” mechanism to facilitate binding to surfaces, with the T4P dwell time increasing from 75 ms to up to ~3 s when the pilus is under tension.[42] Beaussart et al. additionally demonstrated in PA14 that surface contact time plays a direct role in the adhesion force exhibited by cellular EPS, in their case Pel.[41] By increasing the amount of time a cell remains in contact with a surface, the force generated by EPS adhesion also increases, resulting in stronger attachment. In corroboration with this, we have found that in the Δ*pslBCD* mutant, surface attachment is severely hindered *off* of artificial trails. (Fig. 1d, e; ED Fig 6; SI Video 2). While cells are capable of landing *off* trail, they rarely remain attached for more than a few minutes. Thus, while the T4P can bring cells into contact with the surface, without EPS the cells cannot remain on the surface for extended periods of time. Simultaneous force measurements of multiple T4P-saccharide events at high temporal

resolution correlated to real-time cAMP and cdGMP readouts at the same temporal resolution in conjunction with real-time tracking of motility will be useful future experiments.

Not previously discussed, however, is the role that the surface itself, and cellular products deposited onto surfaces, play in facilitating landing and attachment behavior. While the Δ*pslBCD* mutant is unable to attach efficiently *off* trail, the cells almost exclusively attach onto the artificial trails (Fig. 1d, e; ED Fig 6; SI Video 2). Cells are thus capable of exploiting available surface deposited EPS to aid in attachment, even when they themselves are incapable of producing EPS to adhere to surfaces. This highlights the critical roles that EPS plays in facilitating coordinated surface colonization, as while *Pa* explores a surface, they leave behind EPS, which can then influence future cell attachment and behavior. By introducing EPS to a surface, either naturally via cell secretion or artificially, the attachment process can be enhanced.

Supplementary References

65. Lemieux, R. U. & Cipera, J. D. T. The preparation and properties of α-D-glucopyranose 1,2-(ethyl orthoacetate) triacetate. *Can. J. Chem.* **34**, 906–910 (1956).

66. Obata, M. *et al.* Synthesis, characterization and cellular internalization of poly(2-hydroxyethyl methacrylate) bearing α-D-mannopyranose. *Polym. Chem.* **2**, 651–658 (2011).

67. Ruda, A., H. Aytenfisu, A., d'Ortoli, T. A., D. MacKerell, A. & Widmalm, G. Glycosidic α-linked mannopyranose disaccharides: An NMR spectroscopy and molecular dynamics simulation study employing additive and Drude polarizable force fields. *Phys. Chem. Chem. Phys.* **25**, 3042–3060 (2023).

68. Decout, A. *et al.* Deciphering the molecular basis of mycobacteria and lipoglycan recognition by the C-type lectin Dectin-2. *Sci. Rep.* **8**, 16840 (2018).

69. Sauer, M. M. *et al.* Binding of the bacterial adhesin FimH to its natural, multivalent high-mannose type glycan targets. *J. Am. Chem. Soc.* **141**, 936–944 (2019).

70. Kuchma, S. L. & O'Toole, G. A. Surface-induced cAMP signaling requires multiple features of the *Pseudomonas aeruginosa* type IV pili. *J. Bacteriol.* **204**, e00186-22 (2022).

71. Navarro, M. V. A. S., De, N., Bae, N., Wang, Q. & Sondermann, H. Structural analysis of the GGDEF-EAL domain-containing c-di-GMP receptor FimX. *Structure* **17**, 1104–1116 (2009).

72. Kühn, M. J. *et al.* Mechanotaxis directs *Pseudomonas aeruginosa* twitching motility. *Proc. Natl. Acad. Sci. U. S. A.* **118**, e2101759118 (2021).

73. Jain, R., Sliusarenko, O. & Kazmierczak, B. I. Interaction of the cyclic-di-GMP binding protein FimX and the type 4 pilus assembly ATPase promotes pilus assembly. *PLoS Pathog.* **13**, e1006594 (2017).

74. Li, Y. *et al.* Extracellular polysaccharides mediate pilus retraction during social motility of *Myxococcus xanthus*. *Proc. Natl. Acad. Sci. U. S. A.* **100**, 5443–5448 (2003).